Performance Comparison of Reflector- and AESA-based Digital Beamforming for Small Satellite Spaceborne SAR

by

Kevin Gema
GMXKEV001

A dissertation presented in partial fulfilment for the degree of
Masters of Engineering

Supervised by:
Emeritus Professor Michael Inggs
Dr. Mohammed Yunus Abdul Gaffar

Department of Electrical Engineering
University of Cape Town, SA
August, 2019

Acknowledgements

First and foremost I would like to express my sincerest gratitude towards my supervisor Prof. Michael Inggs for his useful comments, remarks and overall guidance throughout this journey of writing a masters dissertation. His wealth of knowledge and enthusiasm for the topic and industry together with his boundless patience, makes Prof. Inggs the ideal mentor and supervisor.

Furthermore, I would like to thank Space Advisory Company for granting me this opportunity to further my studies and apply my knowledge to their technology roadmap.

I would like to thank Dr. Mohammed Yunus Abdul Gaffar for his encouragements, insightful comments and questions, helping to improve the reader's experience.

Last but not least, I would like to thank my parents Elizabeth and Antonio Gema for their support and their roles as proofreaders. Raising an engineer is never easy, but they somehow manage to keep me aligned to the world.

Kevin Gema
Somerset West, South Africa
28 January, 2019

I know the meaning of plagiarism and declare that all the work in the document, save for that which is properly acknowledged, is my own. This thesis/dissertation has been submitted to the Turnitin module (or equivalent similarity and originality checking software) and I confirm that my supervisor has seen my report and any concerns revealed by such have been resolved with my supervisor.

Signed by candidate

Abstract

Spaceborne Synthetic Aperture Radar (SAR) sensors play an ever increasingly important role in Earth observation in the fields of science, geomatics, defence, commercial products and services. The user community requirements for large, high temporal and spatial resolution swaths has driven the need for low-cost, high-performance systems. The increasing availability of commercial launch vehicles shall bolster the manufacturing and industrialisation of a smaller class sensor.

This work deals with the performance comparison between a small satellite class planar array and reflector antenna system. Here the focus lies on digital beamforming techniques for the operation in wide-swath, high-resolution stripmap mode.

For this the sensor sensitivity and ambiguity suppression performance in range and azimuth are derived. The Jupyter notebook environment with code in the Python language served as a convenient mechanism for modelling and verifying different performance aspects. These performance metrics are simulated and verified against existing systems. The limitations the spherical Earth geometry has on the transmitter timing and the imaged scene are derived. This together with the SAR platform orbital characteristics lead to the establishment of antenna design constraints. A planar array and reflector system are modelled with common design specifications and compared to a sea ice monitoring scenario.

The use of digital beamforming techniques together with a high gain reflector antenna surface provided evidence that a reflector antenna would serve as a feasible alternative to planar arrays for spaceborne SAR missions.

Table of Contents

List of Figures

List of Tables

Acronyms and Symbols

Acronyms

acronym	description
AASR	Azimuth-Ambiguity-to-Signal Ratio
ADC	Analogue-to-Digital Converter
AESA	Active Electronically-Scanned-Array
ASAR	Advanced Synthetic Aperture Radar
COTS	Commercial off-the-shelf
CNR	Clutter-to-Noise Ratio
DBF	Digital Beam-Forming
DEM	Digital Elevation Model
ERS	European Remote Sensing Satellite
ESA	European Space Agency
HPBW	Half Power Beamwidth
JERS	Japanese Earth Resource Satellite
LEO	Low Earth Orbit
NASA	National Aeronautics and Space Administration
NESZ	Noise Equivalent Sigma Zero
PRF	Pulse Repetition Frequency
PRI	Pulse Repetition Interval
RADAR	Radio Detection And Ranging
RASR	Range-Ambiguity-to-Signal Ratio
RCS	Radar Cross Section
RF	Radio Frequency
SAR	Synthetic Aperture Radar
ScanSAR	Scanning Synthetic Aperture Radar
SCORE	Scan On Receive
SIR	Shuttle Imaging Radar
SLAR	Side-Looking Airborne Radar
SNR	Signal-to-Noise Ratio
SRTM	Shuttle Radar Topography Mission
SSTL	Surrey Satellite Technology Limited
TRM	Transmit/Receive Module
TWT	Travelling Wave Tube
USSR	Union of Soviet Socialist Republics

Lower Case Symbols

symbol	unit	description
d	m	array element spacing
dc	-	pulse duty cycle
f	Hz	frequency
f_c	Hz	carrier / centre frequency
f_D	Hz	Doppler frequency
f_s	Hz	temporal sampling frequency
i	-	count variable for range intervals
j	-	count variable for range ambiguities
m	-	count variable for azimuth ambiguities

Capital Symbols

symbol	unit	description
A	m^2	physical antenna area
A_c	m^2	clutter area
A_e	m^2	effective antenna area
B	Hz	signal bandwidth
B_D	Hz	Doppler bandwidth
B_γ	Hz	processed azimuth bandwidth
B_p	Hz	transmitted pulse bandwidth
C_{2way}	-	2-way antenna pattern
D	m	antenna diameter in elevation or azimuth / total length of a linear array antenna
D_{SAR}	m	SAR baseline length
F	-	noise figure
G	-	antenna pattern along range direction
G_r	-	receive antenna gain
G_t	-	transmit antenna gain
H_{orb}	m	sensor platform orbital altitude
L_s	-	system losses
M	-	count variable for nadir echo ranges
N_0	WHz^{-1}	noise power density
N	-	count variable for PRF blind ranges

P_{avg}	W	average transmitted power
P_r	W	received (signal) power
P_t	W	transmitted (signal) power
R_0	m	zero-Doppler distance sensor-target
R	m	slant range sensor-target
R_f	m	slant range to far edge of swath
R_n	m	slant range to near edge of swath
RX	-	receive / received / receiving
S_a	W	ambiguity signal power
S	W	desired signal power
T_d	s	coherent integration time
TX	-	transmit / transmitted / transmission
V	ms^{-1}	sensor platform velocity (in azimuth)
W_r	m	slant range swath width

Greek Symbols

symbol	unit	description
γ	rad	look angle with respect to nadir
δ_r	m	slant range resolution
δ_{az}	m	azimuth resolution
δ_{rg}	m	ground range resolution
δ_{SLAR}	m	SLAR resolution
Δ_{az}	m	azimuth displacement
η	rad	incidence angle with respect to surface normal
η_a	-	aperture efficiency
θ_{cone}	rad	cone angle
θ_{int}	rad	integration angle
Θ_{3dB}	rad	half-power beamwidth
Θ_R	rad	half-power beamwidth on receive
Θ_T	rad	half-power beamwidth on transmit
λ	m	wavelength
σ^0	-	radar backscatter coefficient
σ	m^2	target radar cross section
σ_c	m^2	clutter radar cross section
τ_f	s	propagation delay at the far edge of swath
τ_m	s	transmitter timing margin
τ_n	s	propagation delay at the near edge of swath

$\tau_n adir$	s	propagation delay of nadir echo
τ_p	s	transmit pulse length
τ_w	s	scene propagation delay / scene duration
ψ	rad	grazing angle with respect to surface normal

Superscripts and Subscripts

symbol	description
{.}avg	average value of quantity
{.}az	quantity refers to azimuth
{.}el	quantity refers to elevation
{.}min	minimum value of quantity
{.}max	maximum value of quantity
{.}r	quantity refers to slant range
{.}rg	quantity refers to ground range
{.}R	quantity refers to receive case
{.}T	quantity refers to transmit case

Constants and Numbers

symbol	value	unit	description
c_0	299792458	ms^{-1}	speed of light
π	3.14159	-	mathematical constant
μ	398600.4418	$\mathrm{km}^3\mathrm{s}^{-2}$	Earth's standard gravitational constant
k	$1.38064852 \times 10^{-23}$	JK^{-1}	Boltzmann's constant
R_E	6378137	m	WGS84 Earth radius at the equator
T_0	290	°K	noise temperature at room temperature

1 Introduction

Spaceborne Synthetic Aperture Radar (SAR) systems have become a mainstay of modern-day Earth observation missions. Since conception, these imaging radars are continually applied to a number of successful missions. With applications ranging from the generation of Digital Elevation Models (DEM), global resource and disaster monitoring, generation of commercial products and services to defence and reconnaissance missions, SAR satellites have made large contributions to the fields of science, security and economy. Cost in terms of resources and complexity has historically been the main factor why space flight and the launch of satellites were limited to powerful government entities and large international collaborations. Even so, the acquisition and processing of SAR data has over the years become more and more commercially viable.

With significant progress made on the performance and miniaturisation of technologies such as processors, storage devices, Analogue-to-Digital Converters (ADC) and Radio Frequency (RF) sources, smaller classes of satellites are more frequently being used for Earth observation. These small satellites, or *smallsats*, are typically constructed using low-cost, Commercial Off-The-Shelf (COTS) components instead of the more expensive, and often restricted, space-grade, radiation-hardened components. This allows for shorter development and testing cycles. Together with the increase in availability of private and commercial launch vehicles, developed by companies such as SpaceX, Blue Origin and Rocket Lab, smallsat SAR systems have sparked the interest of the commercial user community. This is evident by the increasing number of private companies developing SAR sensors for space use and from the first in-orbit demonstrations of smallsat class SAR sensors in 2018 by UK-based company, Surrey Satellite Technology Limited (SSTL) and Finnish company, ICEYE Oy. These smallsat SAR sensors are envisioned to form part of multi-satellite constellations providing continuous, all-weather, day-and-night, high resolution global coverage.

The smallsat drivers - cost, size, complexity and mass - are the reasons behind the feasibility study of utilising reflector antennas for SAR missions instead of the more widely used Active Electronically Scanned Array (AESA) antennas. Spaceborne reflector antenna systems benefit from mature technology adopted from military communication satellites. They feature less expensive, easy to manufacture and robust components, making for better thermal and radiation shielding as well as easier integration onto the satellite bus structure. AESA systems however, provide inherent redundancy, consisting of many transmitter and receiver elements, allowing for the graceful failure of individual radiators with minimal impact on the overall system performance. Compared to this, reflector systems typically use one or more radiator elements, creating single points of failure in the overall system.

Beamforming refers to the shaping and steering of the antenna beam patters. With analogue signals this was done using phase shifters and attenuators per radiator element or columns of radiators together, which allowed for the "steering" of the antenna beam off the antenna boresight direction.

Digital Beamforming (DBF) makes use of modern high-speed ADCs together with software and hardware techniques to shape and steer the antenna beam patterns. Spaceborne SAR sensors using DBF can create complex imaging geometries to cover a wide range of applications.

1.1 Motivation and Topicality of Work

Spaceborne SAR sensors have a rich history with the first civilian mission, Seasat launched in 1978 [1]. The objective of the Seasat SAR sensor was the monitoring of oceanographic features and phenomena and utilised a single polarisation, 1024-element, passive microstrip phased array antenna at L-band [2]. The sensor covered a swath width of 100 km in stripmap mode. Seasat formed the basis for future mission concepts and designs and paved the way for the use of SAR on the early Space Shuttle missions, designated as the Shuttle Imaging Radar (SIR) missions.

The Shuttle missions allowed for the development and demonstration of increasingly complex SAR imaging systems, including SIR-A, 1981, SIR-B, 1984, and two SIR-C/X missions in 1994 [3]. SIR-A and SIR-B used the same antenna technology as Seasat, with the additional capability of mechanically steering the antenna in elevation on SIR-B [4]. The SIR-C/X missions made use of many low-power solid state transmitters instead of a single high-power transmitter, and also featured multi-polarisation. The antennas could perform electronic beam steering in elevation, negating the need for the mechanical steering. The second SIR-C/X mission had nearly the same orbit as the first, which allowed for repeat-pass interferometric SAR processing in L, C and X-band [5].

The SIR-C phased array was the first to allow for Scanning Synthetic Aperture Radar (ScanSAR) and spotlight modes [5]. In ScanSAR the antenna beam is steered in elevation to cover different sub-swaths, allowing for wider ground swath coverage at lower azimuth resolution. In spotlight mode, the antenna beam is steered to dwell on a fixed position, increasing the azimuth resolution and radiometric sensitivity but at the expense of swath width.

The X-band sensor on SIR-C/X, named X-SAR, made use of a slotted waveguide antenna with a Travelling Wave Tube (TWT) amplifier, allowing for higher transmitter power than microstrip antennas. Slotted waveguides have since been used on numerous spaceborne SAR missions, including the European Remote Sensing Satellites (ERS), ERS-1, 1991 [6] and ERS-2, 1995 [7], which served as the European Space Agency's (ESA) first Earth observation program. Others include the Russian (USSR) Almaz-1, 1991 [8], which served as a reconnaissance satellite, the Japanese Earth Resource Satellite 1 (JERS-1), 1992 [9], combined SAR and optical sensors, the American/German Shuttle Radar Topography Mission (SRTM), 2000 [10] generated the first near-global DEMs.

The innovation of various RF sources led to the adoption of small Transmit/Receive Modules (TRM) for use in active phased array antennas. Each of these TRMs were individually powered and controlled, allowing for improved beamforming and steering capabilities, giving rise to the name Active

Electronically Scanned Arrays. SAR satellites such as ESA's Envisat Advanced Synthetic Aperture Radar (ASAR), 2002 [11], and Canada's RADARSAT-2, 2007 [12], made use of these AESA antennas for the observation of Earth dynamic systems. RADARSAT-2 is still operational and finds extensive use in the monitoring of sea ice conditions. Germany's observation SAR systems TerraSAR-X, 2007 [13], and TanDEM-X, 2010 [14], also make use of AESA systems allowing for the generation of high resolution interferometric DEMs of the Earth's surface.

Reflector antennas found their first use in military communications satellites. The first reflector-based SAR system were used by the USSR in the Venera 15 and 16 missions, 1983 [8], to map the surface of Venus. Other SAR missions such as the Cassini-Huygens mission, 1997 [15], as a collaboration between the National Aeronautics and Space Administration (NASA) and ESA was intended to map the surface of Saturn's largest moon, Titan. Reflector SAR systems were often used in surveillance satellites such as the German SAR-Lupe constellation, 2006-2008 [16], and the Israeli TecSAR satellite, 2008 [17].

For commercial use cases, the cost of manufacturing and launching multiple satellites is a constraint. Therefore, development tends towards the use of wide-swath, high resolution, short revisit-time operational modes. For wide swaths broad transmit beams are required. For high azimuth resolution, high Pulse Repetition Frequencies (PRF) are required. These two requirements are unfortunately contradictory, and lead to ambiguities in the imaged scene. One solution to mitigate this problem is to make use of DBF and smart receiving modes such as Scan-On-Receive (SCORE), where the narrow receive beam follows the transmitted pulse along the ground. These techniques have been investigated in depth [18]–[21], including DBF for reflector systems [22]–[24].

1.2 Scope of Work

The work investigated various performance metrics for detailing spaceborne SAR image distortions caused by ambiguous signal returns. The investigation, based on the work presented by Younis et al. in [18], focused on comparing these performance metrics between an AESA antenna system and an equivalent reflector antenna system. The scope of this work covered the derivation of the imaging boundary conditions along with the mathematical models for the ambiguity metrics. Finally the models were coded into Jupyter notebooks to perform the required comparison.

Assumptions made in this work include:

- A SAR platform with constant altitude and velocity
- Uniform target reflectivity throughout the imaged scene
- Modelling with the use of un-tapered antenna patterns
- Modelling the reflector antenna as a uniformly illuminated rectangular aperture
- No distortions to the antenna patterns at different elevation angles

- Stripmap mode operation with beamsteering in elevation

Research objectives:

- Derivation of spaceborne SAR imaging boundary constraints on PRF
- Derivation of spaceborne SAR imaging sensitivity and ambiguity performance metrics
- Verification of derived parameters against published results
- Modelling and comparison of equivalent AESA and reflector systems for the monitoring of sea ice

The accurate modelling of antenna field distribution models and signal processing of SAR imagery fall outside this scope of this work.

1.3 Contribution

Considering the current state of technological advances, this work contributes towards the performance comparison of AESA and reflector systems. The work is based on the study done by Younis et al. [18], with the aim of implementing software modules and libraries for the analysis of different antenna performance metrics. Focused on the utilisation of DBF for stripmap operational use in SAR systems.

The Jupyter environment with the Python kernel was chosen as an ideal platform for rapid system modelling and verification. Jupyter presents developers with a document-style coding interface, or *notebooks*, in which code can be split across multiple *cells*. Users are able to make use of the Markdown language syntax and LaTeX formatted equations to create an interactive document with live code, visualisations, equations and narrative text [25]. This allows for the creation of richly formatted, shareable documents containing not only data sets and graphics, but also the code to dynamically change parameters at run-time to reconfigure data and output products.

The use of Jupyter together with Python allowed for the creation of a reconfigurable and dynamic tool for rapid system design and validation.

1.4 Overview of this Work

Chapter 1 states the motivation and objective of this study, giving the reader the required background and context needed for further reading.

Chapter 2 covers the fundamental principals of spaceborne SAR imaging geometries and the theoretical background on the different system performance metrics for designing these spaceborne SAR platforms. The chapter starts with the establishment of the imaging resolution cell in both azimuth

and range, focusing on the differences between airborne SAR and spaceborne SAR systems. Further the chapter covers sampling theory, establishing the relationship between the SAR platform orbital characteristic such as altitude and velocity to the Doppler bandwidth and receiver sampling frequency.

For the discussion on SAR image quality and the different ambiguities or distortion which might arise, the Signal-to-Noise Ratio (SNR) for the pulse-Doppler technique is derived from the expression of the radar received power. This SNR expression is expanded to give the definitions for the Clutter-to-Noise Ratio (CNR) and the Noise-Equivalent Sigma Zero (NESZ). These parameters together with the spatial resolution form the basis requirement for nearly all SAR missions.

To evaluate the level of distortion in SAR images due to the finite sampling of the Doppler spectrum, the expression for the Azimuth-Ambiguity-to-Signal Ratio (AASR) is derived. For the measurement of distortion created by the simultaneous reception of coincident pulses - preceding and succeeding pulses- the expression for the Range-Ambiguity-to-Signal Ratio (RASR) is presented. These ambiguities are mitigated by compensating antenna designs and by intelligent selection of the PRF.

The choice of PRF is further constrained by the combination of imaging geometry, transmission events and nadir echo returns. The limitations on the minimum and maximum PRF are derived together with the valid ranges where no eclipsing of the radar receiver occurs.

These concepts are utilised in succeeding chapters to verify the design choices, measure and compare the image performance aspects of both AESA and reflector systems.

In Chapter 3 the designed code models are verified against published results. A detailed study of available technical reference documentation is done, and scenarios, where the required level of technical specification were available, are chosen to verify the various performance aspects of the respective systems. Due to the nature of the operational use cases, and studies performed during these use cases, their configurations, imaging geometries, type of analysis performed on the SAR data, published measurements vs. simulated measurements, publication platforms, and many other factors, hardly any material exists with all the required information in a single location.

The performance metrics published in studies are usually limited to a specific use case, with a limited geometry and limited measured data. This is an understandable consequence of spaceborne systems, in which the SAR platform is constrained not only by users competing for uptime on the system, but also by power and downlink budgets. These limit the capture time, location and downlinking opportunities during which data can be acquired and analysed. In many cases the published performance results are either presented as a single figure, as is usually the case with the ambiguity suppression ratios, or as a detailed graph with ambiguous mathematical derivation.

To verify the software models for the antenna designs, and the performance metrics of the intended systems, case studies from literature are chosen in which little or no assumptions had to made on the

design and layout of the respective systems. This is particularly important for the antenna designs, since most of the performance metrics stem directly from the antenna radiation pattern and other antenna characteristics.

For the planar array system, two scenarios are chosen. The first scenario is based on the conceptual AESA design described by Younis et al. [18] for a narrow-swath stripmap imaging mode. Here, a single wide beam in elevation is utilised during transmission (TX), with a narrow beam on reception (RX). The TX beam is formed using a subset of the elements in elevation and all elements in azimuth. For the RX beam all elements were used in elevation and azimuth. This results in a stripmap of approximately 125 km in ground-range, and the performance metrics are analysed over the incidence angle ranges of 32.1° to 40.6°. The TX and RX antennas are modelled separately and the measured values calculated include NESZ, AASR and RASR. These are compared against the results published in [18].

For a second scenario, a RADARSAT-2 wide-swath configuration utilising 3 beams on transmission and making use of SCORE for the receive antenna is chosen. This scenario makes use of 3 separate beams on transmission with the intent of covering a 440 km ground-swath width while retaining high spatial resolution in both azimuth and elevation. Each of the three TX beams cover different sub-swath sizes, and therefore each TX beam is modelled separately with a different number of active elements in elevation to create the required beamwidths. A single RX beam is modelled utilising the entire planar array. This RX beam makes use of SCORE to steer across the entire illuminated swath over the incidence angle range of 20° to 45°. The NESZ, AASR and RASR values for each sub-swath are calculated and compared against the results published in [26] and [27].

In contrast to the planar array system, not many published results are available for the verification of a spaceborne multi-feed reflector SAR system. Few publicly known reflector systems such as SAR-Lupe and TecSAR have been launched and have published some performance metrics. However, too few technical designs specifications are available in the public domain to model the reflector systems without making assumptions on key design aspects. These satellites are utilised for reconnaissance missions, and hence the lack of published technical specifications are understandable and to be expected.

Therefore the model verification of the reflector-based design focuses around the conceptual model described in [18]. This system makes use of 26 TRMs in elevation with a single channel in azimuth. Simplified antenna models are used in this dissertation for the TX and RX patterns, with all feed elements activated and illuminating a portion of the reflector during transmission resulting in a wide swath. On reception the entire reflector is illuminated but focused on individual feed elements. Each element illuminates a particular sub-swath on the ground, and so DBF on receive is performed by selectively switching on the feed element corresponding to the sub-swath illuminated during the sub-interval of the Pulse Repetition Interval (PRI) as the transmitted pulse travels along the ground.

Verification is limited to the stripmap operational mode in which the TX beam illuminates a 125 km swath over the incidence angle ranges of 32.1° to 40.6° at a spatial resolution of 6 m. The NESZ, AASR and RASR values are calculated and compared against those published in [18].

Chapter 4 details the design and performance comparison of the planar array and reflector systems for the application of sea ice monitoring. This use case imposes different requirements on the SAR system depending on which aspects of sea ice are investigated, such as ice type classification, ice drift monitoring, ice thickness and melt detection [28]. Research has been done on the trade-off of radar parameters such as centre frequency, spatial resolution and polarisation to determine how sea ice parameters influence radar scattering [28]. From this a set of common parameters and user performance requirements are selected for the system comparison. These are listed in Table 4.1.

Figure 1.1 shows various ice types imaged at different frequencies in a region of the Baltic Sea close to the Swedish coast between 60° and 65° latitudes [29].

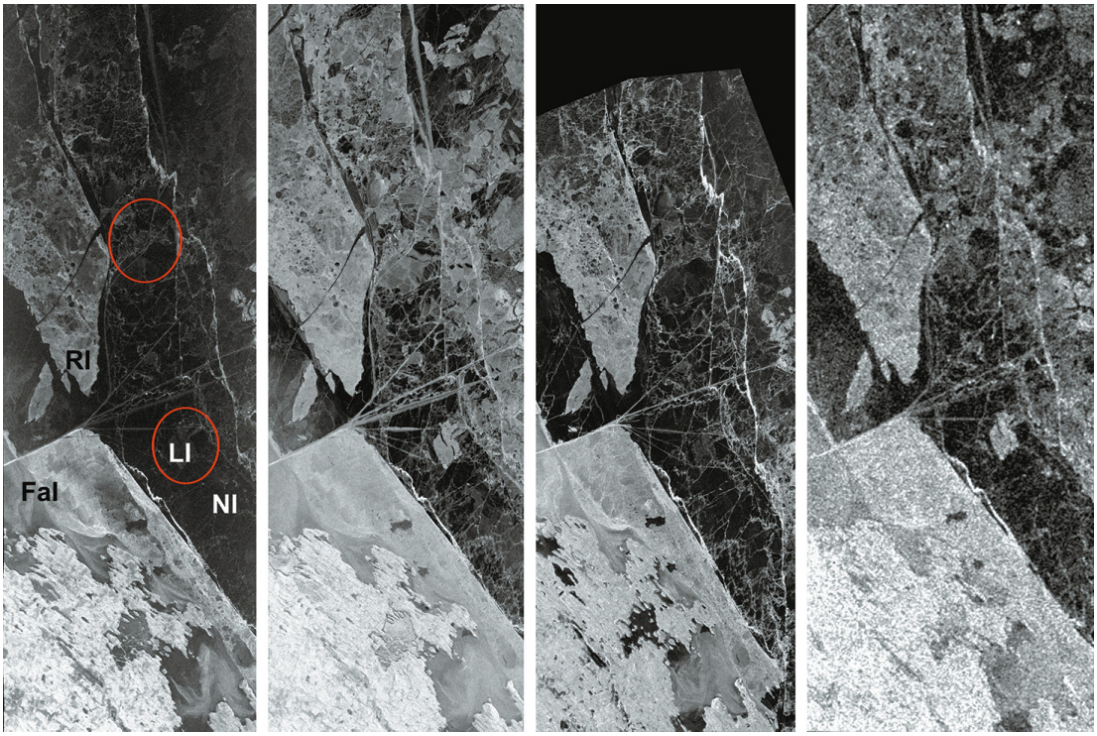

Figure 1.1: Sea ice observed at different frequencies. From left to right: TerraSAR-X, HV-polarisation; TerraSAR-X, HH-polarisation; PALSAR, HH-polarisation; and ASAR, HH-polarisation. The red ellipses indicate level ice (LI) characterised by backscatterring coefficients that are sensitive to frequency and polarisation. Fast ice (FaI), new ice (NI) and rough ice (RI) are also indicated. Image obtained from [29].

The two left-most images were taken at X-band with HV and HH polarisation respectively. The third image was taken at L-band using HH polarisation and the last at C-band using HH-polarisation. Variations in the imagery occur at local scale, with clear differences between HV and HH polarisation at X-band [29]. The radar acquisitions occurred on 19 and 20 February 2009 from TerraSAR-X,

ALOS PALSAR and Envisat ASAR. In these figures the radar return for level ice is fairly high for single polarisations but low at cross-polarisations. The X-band HV polarised image corresponds closely to the L-band image and the X-band HH-polarised image corresponds closely to the C-band image. The SNR level for the X-band cross polarised image is lower than the L-band image. At X-band finer structure details are more clearly visible than at L-band and C-band.

The chapter starts by investigating the effects of orbital altitude on the choice of look angles as shown in Figure 4.1. Except for the effects that a spherical Earth model has on the imaging geometry, other factors such as cost, both in terms of development time and component selection, mass and the availability of commercial launch vehicles impose upper and lower limits to usable satellite orbits. Together with the requirement of high repeat cycles, Low Earth Orbits (LEO), specifically sun synchronous orbits, reduce the mass and power requirements imposed on satellites by placing the satellite in near constant sunlight. This allows the solar panels to work continually, mitigating the need for large batteries. An added benefit of sun synchronous orbits is that every time the satellite is overhead, the surface illuminating angle beneath the satellite is nearly the same. These conditions are ideal for continual stripmap operation with beamsteering only required in the elevation direction (cross-track) to illuminate at the desired incidence angle ranges.

Further, the designs for the planar and reflector systems are derived in sections 4.2 and 4.3, which are mainly the antenna specifications. A PRF analysis is done to ensure the antenna specifications and choice of system parameters were valid. The results are shown in Figure 4.2. With the verified parameters, each system's performance metrics - NESZ, AASR and RASR - are modelled and illustrated in Figures 4.5 to 4.7. Many of the specified performance metrics measure the impact of distortions caused by the antenna sidelobes, which are modelled by including the antenna pattern shape into the equations for the performance metrics.

Initial assumption on performance is that the AESA system would outperform the reflector-based antenna, since its antenna pattern can be accurately synthesised and therefore utilises a very narrow receive beam, steered across the swath on reception, yielding high signal returns. However, with the reflector antenna illuminated by a feed array consisting of multiple TRMs, DBF is used during transmission and reception by activating individual feed elements [18]. During transmission, all feeds are activated, illuminating a sub-section of the reflector surface, at low gain, which in turn allows for illumination of a wide swath. During reception the entire reflector surface is used, and therefore very high gain, but the return signal is focused on individual feed elements. The receive elements are activated as the transmitted pulse travels along the ground.

The combination of simpler design, significant reduction in manufacturing costs, and the use of a large reflector surface to boost the receiver gain, makes the reflector system a contender to the planar array.

Chapter 5 presents the conclusions and recommendations from the analysis done in this dissertation.

2 Theoretical Background

This chapter provides an overview of the necessary SAR fundamentals - resolution, signal sampling, signal-to noise ratio, clutter-to-noise ratio and noise-equivalent sigma zero - required to evaluate the performance of spaceborne SAR systems. A spherical Earth model was used in all calculations, and so a relationship was established between the SAR platform's altitude and orbital velocity to Doppler bandwidth and PRF. Following these derivations, the ambiguities present in SAR images due to strong returns received by the antenna sidelobes were introduced. The ambiguity effects were illustrated and their mathematical representations were established, i.e. AASR and RASR. The part of this chapter presents an overview of the limitations on the choices of PRF values and the constraints these limitations placed on the SAR systems.

2.1 Synthetic Aperture Radar Resolution

The transmission and reception of electromagnetic energy by the SAR forms 2D imagery representing a reflectivity map of the imaged scene, with bright spots for backscattered signals and darker areas for forward scattered signals or shadowed regions as shown in Figure 2.1.

Before the use of spaceborne SAR systems, Side-Looking Airborne Radars (SLAR) were used for imaging, but they suffered from inferior azimuth resolution and a range resolution which degrades as the slant range increases. Figure 2.2 illustrates the SLAR imaging geometry. Resolution refers to the smallest separation between distinctly detectable targets. For a SLAR system with an azimuth antenna beamwidth Θ_{az}, given by Equation 2.1 [30], which is dependent on the radar wavelength λ, and the physical antenna length in azimuth D_{az}, the azimuth resolution $\delta_{SLAR,az}$, is given by Equation 2.2 [30]. It is noteworthy that the SLAR azimuth resolution is dependent on the slant range distance, R_0, between the radar platform and the imaged scene and as well as the physical antenna length in azimuth.

$$\Theta_{az} = \frac{\lambda}{D_{az}} \tag{2.1}$$

$$\delta_{SLAR,az} = \frac{\lambda}{D_{az}} R_0 = \Theta_{az} R_0 = \frac{H_{orb}\lambda}{D_{az}\cos\gamma} \tag{2.2}$$

H_{orb} is the SAR platform altitude and γ is the look angle with respect to nadir. The slant range resolution for a SLAR system $\delta_{SLAR,r}$, is given by Equation 2.3 [30] which is only dependent on the signal bandwidth, B. However, the ground range resolution $\delta_{SLAR,rg}$, given by Equation 2.4, is determined by the slant range resolution divided by the sine of the look angle γ, and is dependent

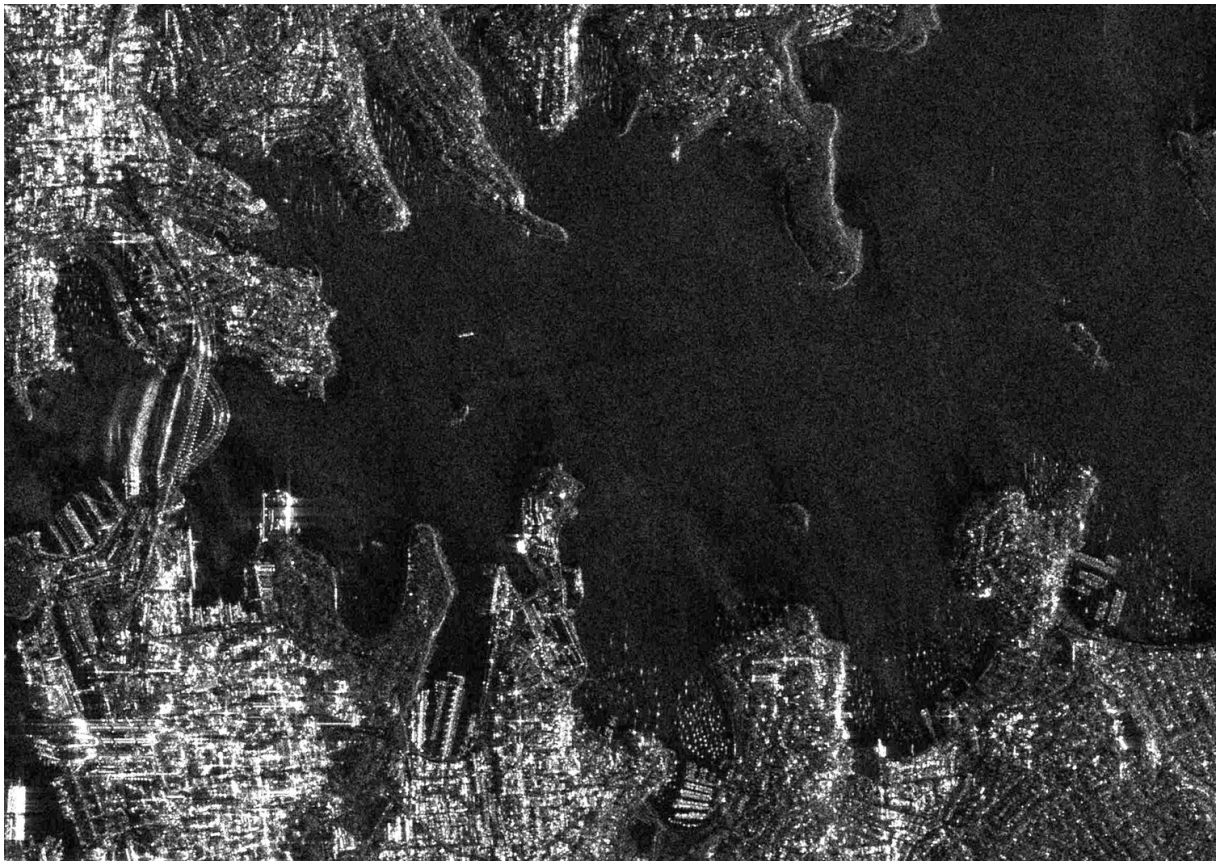

Figure 2.1: S-band SAR image over Sydney Harbour, Australia, acquired in November 2018 by the SSTL NovaSAR-1 satellite. Image obtained from: *https://www.sstl.co.uk/media-hub/latest-news/2018/sstl-releases-first-images-from-s-band-synthetic-a*.

on the slant range to the scene. c_0 refers to the speed of light.

$$\delta_{SLAR,r} = \frac{c_0}{2B} \tag{2.3}$$

$$\delta_{SLAR,rg} = \frac{c_0}{2B\sin\gamma} = \frac{c_0}{2B\sqrt{1-(H_{orb}/R_0)^2}} \tag{2.4}$$

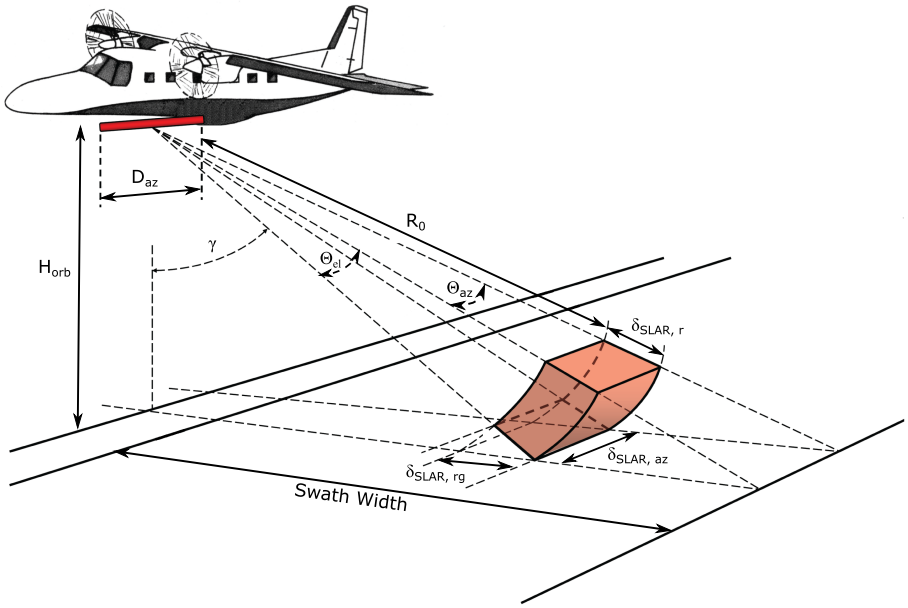

Figure 2.2: Side-Looking Airborne Radar imaging geometry. Image adapted from *http://www.seos-project.eu/modules/marinepollution/marinepollution-c02-s02-p01.html*.

Conversely, SAR azimuth resolution δ_{az}, is approximated by Equation 2.5 and is independent on slant range and only dependent on the antenna dimensions in azimuth [30]. The azimuth beamwidth Θ_{az}, stays the same as in Equation 2.1.

$$\delta_{az} = \frac{D_{az}}{2} \tag{2.5}$$

Slant range resolution δ_r, is given by Equation 2.6, which is only dependent on the receiver bandwidth, as is the case in Equation 2.3.

Figure 2.3 illustrates a monostatic spaceborne SAR configuration. The SAR platform's flight direction is denoted as *azimuth* and the line-of-sight direction between the SAR system and the observed area on the ground as *slant range*. With the side-looking geometry employed in SAR systems, the ground range resolution is dependent on the look angle and given by Equation 2.7 [30].

$$\delta_r = \frac{c_0}{2B} \tag{2.6}$$

$$\delta_{rg} = \frac{\delta_r}{\sin\gamma} = \frac{c_0}{2B\ \sin\gamma} \tag{2.7}$$

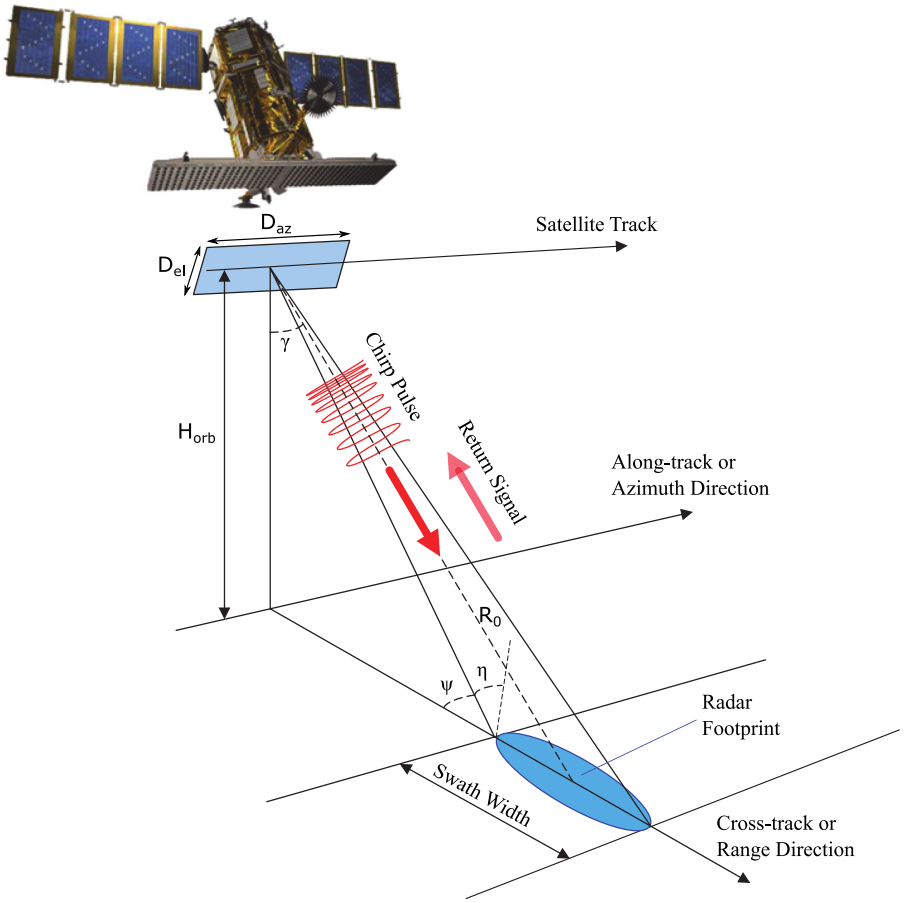

Figure 2.3: A typical spaceborne SAR geometry with the definition for the Azimuth (along-track) direction parallel with the flight direction of the satellite and the Slant Range (cross-track) direction perpendicular to this flight direction. Ground Range is the distance between the nadir point of the satellite and the observed swath. The SAR footprint is shown together with the swath width and local incidence angle. Image adapted from [31].

2.2 Signal Sampling

Coherent processing is performed on the return echoes from a sequence of transmitted electromagnetic pulses along the cross-track dimension under the assumption that the SAR platform velocity, V, is much smaller than c_0. As the platform propagates along its flight path, a new one-dimensional set of data is collected and processed. Therefore the SAR signal returns in the azimuth direction are inherently discreet. Sampling of the signals returns must therefore satisfy the Nyquist-Shannon sampling criterion, with the receiver sampling rate twice that of the highest frequency. The receiver therefore needs to sample at least at the Doppler bandwidth, B_D, of the image scene:

$$f_s \geq 2f_{max} \; = \; B_D \tag{2.8}$$

The Doppler bandwidth can be expressed in terms of the SAR platform velocity, V, as shown in Equation 2.9 [32, p. 21]. The expression for the platform velocity, using a spherical WGS84 Earth model, is given by Equation 2.10

$$\begin{aligned} B_D &= f_{D,high} - f_{D,low} \\ &= (2V/\lambda)\left[\sin(\Theta_{az}/2) - \sin(-\Theta_{az}/2)\right] \\ &\approx \frac{2V\Theta_{az}}{\lambda} \end{aligned} \tag{2.9}$$

$$V = \sqrt{\frac{\mu}{R_E + H_{orb}}} \tag{2.10}$$

μ is the Standard Gravitational Parameter $\approx 398600.4418\ km^3/s^2$ and R_E is the radius of the Earth $\approx 6378\ km$ at the equator. $f_D = 2(V\sin\theta)/\lambda$ is the Doppler shift relative to the transmitted frequency and θ is the angle of the target off boresight [32, p. 17].

2.3 Signal-to-Noise Ratio

The expression for the SNR is used to derive the expressions for both the CNR and NESZ, and therefore deserves some attention here. The starting point for all of these metrics is the well-known expression for the radar received power given by Equation 2.11 [30].

$$P_R = \frac{P_T G_T G_T \lambda^2 \sigma}{(4\pi)^3 R^4 L_s} \tag{2.11}$$

P_T is the transmitted power, G_T and G_R are the transmitted and received antenna gains, σ is the target Radar Cross Section (RCS), R is the sensor to target slant range and L_s represents the system losses. The antenna gains are given by Equation 2.12. $A_e = A \cdot \eta_a$ is the effective antenna area, A is the physical antenna area and η_a is the antenna aperture efficiency.

$$G = \frac{4\pi A_e}{\lambda^2} \tag{2.12}$$

Since SAR data acquisition and image formation are coherent processes, the pulse-Doppler radar range equation for SNR given by Equation 2.13 is a preferred starting point [30]

$$SNR = \frac{P_T\ dc\ G_T A_e \sigma}{(4\pi)^2 R^4\ kT_0\ F L_s B_D} \tag{2.13}$$

dc is the transmitter duty cycle, k is Boltzmann's constant, $T_0 = 290^\circ\ K$ is the standard temperature, F is the system noise figure and B_D is the Doppler bandwidth. This expression is simplified by substituting in:

- The average power, $P_{avg} = P_T dc$
- The aperture gain on receive, $G_R = 4\pi A_e/\lambda^2$
- The thermal noise power spectral density, $N_0 = kT_0F$
- The coherent integration time (dwell time), $T_d = 1/B_D$

Resulting in Equation 2.14 [30]

$$SNR = \frac{P_{avg}G_TG_R\lambda^2\sigma T_d}{(4\pi)^3\ R^4N_0L_s} \tag{2.14}$$

The relevant SAR expression for dwell time in squinted geometries is given by Equation 2.15 [30] with D_{SAR} the SAR baseline length and θ_{int} the azimuth integration angle.

$$T_d = \frac{R\lambda}{2V\sin\theta_{cone}\delta_{az}} \tag{2.15}$$

For un-squinted geometries, the cone angle, $\theta_{cone} = 90^\circ$. Substituting Equation 2.15 into Equation 2.14 gives the expression for SNR for the pulse-Doppler image formation [30]:

$$SNR = \frac{P_{avg}G_TG_R\lambda^3\sigma}{2V\sin\theta_{cone}\ (4\pi)^3\ R^3\ N_0L_s\delta_{az}} \tag{2.16}$$

2.4 Clutter-to-Noise Ratio

A required property in SAR applications is the surface scattering value, referred to as clutter in normal radar systems. The CNR is computed from the SNR by replacing the point target RCS value with that of a clutter patch, $\sigma_c = \sigma^0 A_c$, with the down-range and cross-range resolutions [30]. The clutter area, A_c, is given by

$$A_c = \delta_{az}\left(\frac{\delta_r}{\cos\psi}\right) \tag{2.17}$$

ψ is the grazing angle at the clutter patch. Substituting these values into Equation 2.16 yields the equation for CNR given by Equation 2.18

$$CNR = \frac{P_{avg}G_TG_R\lambda^3\sigma^0\delta_r}{2V(4\pi)^3R^3N_0L_s\sin\theta_{cone}\cos\psi} \tag{2.18}$$

2.5 Noise-Equivalent Sigma Zero

NESZ is a key measurement of the sensitivity of a SAR system at which the surface backscatter coefficient, σ^0, is measured when the signal power equals the system noise power. More accurately, it refers to the value of the backscatter coefficient which provides a terrain reflectivity, or clutter power, equal to the thermal noise. This backscatter coefficient is found by setting Equation 2.18 to 1 and solving for σ^0 as shown in Equation 2.19 [18], [30].

$$NESZ \;=\; \sigma^0 \;=\; \frac{2V(4\pi)^3R^3N_0L_s\sin\theta_{cone}\cos\psi}{P_{avg}G_TG_R\lambda^3\delta_r}\cdot\Upsilon \tag{2.19}$$

Where $\Upsilon = f\left(C_{el}(\theta), C_{az}(\phi), R(\phi,\theta)\right)$ represents the two-way antenna beam pattern shapes and is a function of elevation, azimuth and slant range [18]. Substituting the ground range resolution, $\delta_{rg} = \delta_r \;/\cos\psi$, into Equation 2.19 yields the NESZ as

$$NESZ \;=\; \frac{2V(4\pi)^3R^3N_0L_s\sin\theta_{cone}}{P_{avg}G_TG_R\lambda^3\delta_{rg}}\cdot\Upsilon \tag{2.20}$$

2.6 Range-Ambiguity-to-Signal Ratio

Range ambiguities are induced by the simultaneous return and reception of different transmitted pulses. When the sidelobes of a transmitted pulse illuminate high reflectivity targets, the signal returns from these sidelobes are strong enough to be received by the SAR system and overlap with the main beam return from consecutive pulses [32], [33]. This overlapping of return signals on reception causes a duplication of image detail along the range direction as illustrated in Figure 2.4 and Figure 2.5. The timing geometry for transmitted pulses along the range direction with overlapping signals in the record window is shown in Figure 2.6.

The RASR is a measurement of the distortion of the desired signal return with the echoes from preceding and succeeding pulses returning simultaneously at the radar receiver [32]. The measured range information cannot solely be attributed to one specific transmitted pulse, and is therefore ambiguous.

The mathematical expression for the integrated RASR, which represents the ratio between the summation of all the preceding and succeeding pulses within the recording window, and the summation of all the desired signal returns, is given by Equation 2.21

$$RASR = \sum_{i=1}^{N} S_{a_i} \Big/ \sum_{i=1}^{N} S_i \tag{2.21}$$

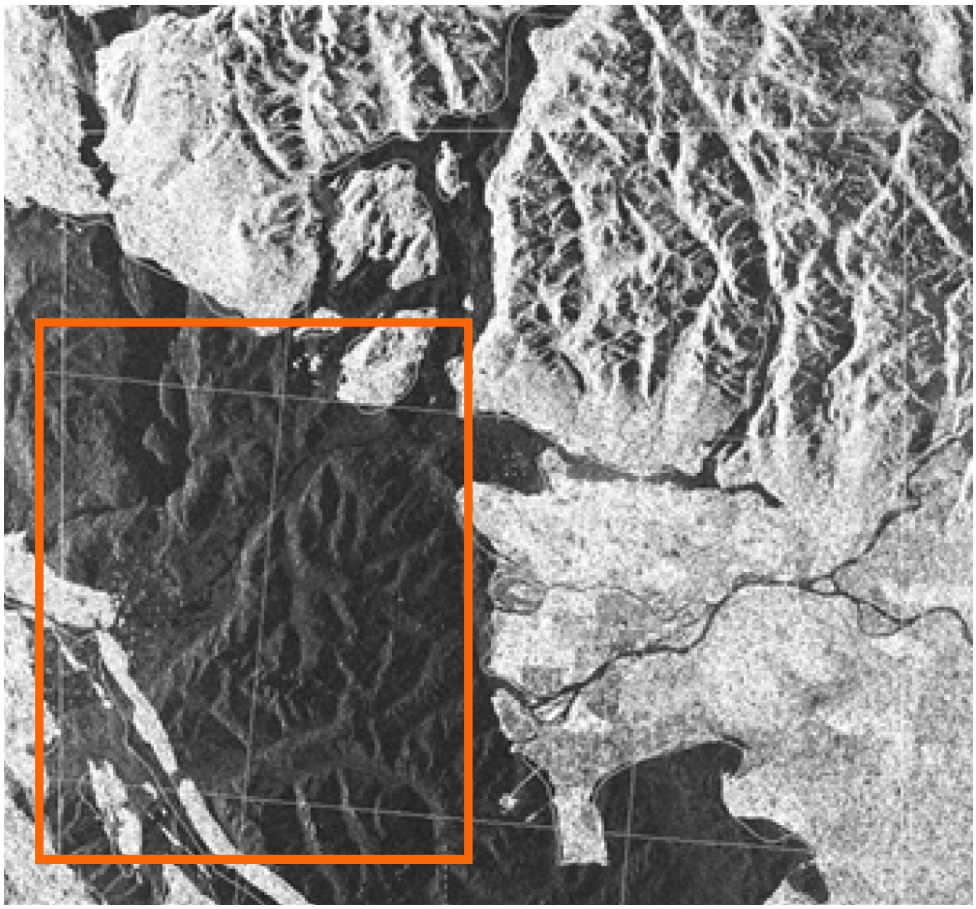

Figure 2.4: Range ambiguities obtained from RADARSAT-1 SAR, beam EH1. Image obtained from [33].

S_{a_i} is the ambiguity signal power for each slant range represented by the index i. S_i is the desired signal power for each slant range with index i. The expressions for each of these are given by Equation 2.22 and Equation 2.23.

$$S_{a_i} = \sum_{\substack{j=-n_h \\ j\neq=0}}^{n_h} \sigma^0_{ij} G^2_{ij} / R^3_{ij} \sin(\eta_{ij}) \qquad \text{for } j \neq 0 \tag{2.22}$$

$$S_i = \sigma^0_{ij} G^2_{ij} / R^3_{ij} \sin(\eta_{ij}) \qquad \text{for } j = 0 \tag{2.23}$$

σ^0_{ij} is the normalised backscatter coefficient at a given incidence angle, η_{ij}, and slant range, R_{ij}. G_{ij} is the antenna pattern along the range direction for a given incidence angle. The slant range positions of the ambiguities are given by Equation 2.24 [32]

$$R_i \;=\; R_0 \;+\; i \cdot \frac{c_0}{2PRF}, \qquad i \in \{-N_N, ..., -1, 1, ..., N_F\}, i \neq 0 \tag{2.24}$$

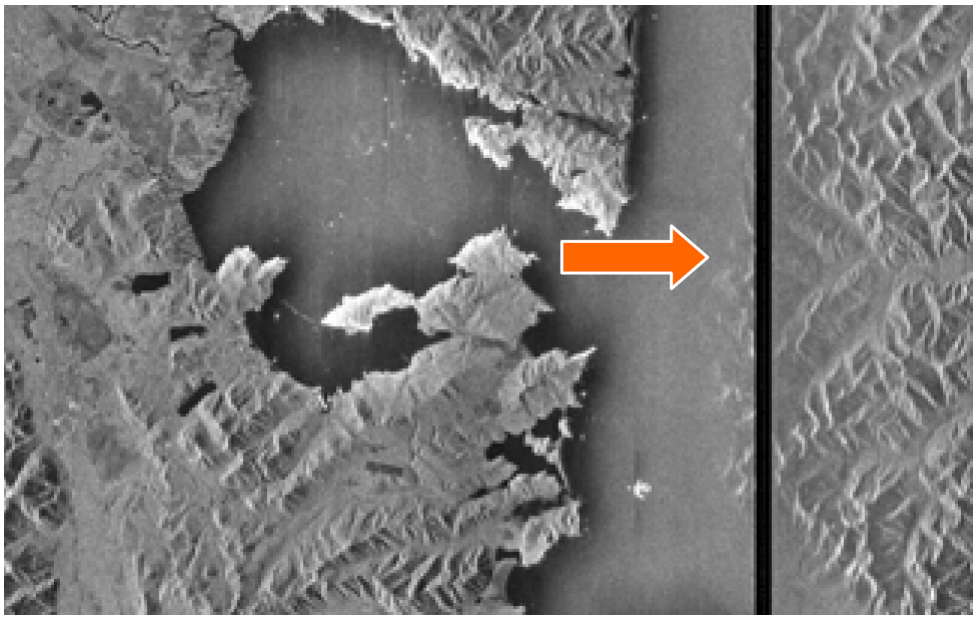

Figure 2.5: Range ambiguities obtained from SAR on Almaz-1. Orbit 2371, Petropavlocsk-Kamchatsky site. Image obtained from [33].

R_0 is the slant range corresponding to the desired echo. The expression in Equation 2.21 is similar to the equation given by Younis et al. [18], where the backscatter coefficient terms cancel out and the RASR can be evaluated as a function of slant range and incidence angles, shown in Equation 2.25. This expression was used for modelling.

$$RASR(R) = \frac{R^3 \sin\eta}{\mid C_{2way,el}(\theta) \mid^2} \sum_{\substack{j\neq 0 \\ j=-N_N}}^{N_F} \frac{\mid C_{2way,el}(\theta_j) \mid^2}{R_j^3 \sin\eta_j} \tag{2.25}$$

$C_{2way,el}(\theta) = C_{T,el}(\theta) \cdot C_{R,el}(\theta)$ is the 2-way antenna field pattern in elevation (range direction), θ is the beam steering angle in elevation, η is the local incidence angle. N_N and N_F are the number of preceding and succeeding ambiguities respectively. The subscript j denotes the index values associated with the ambiguities.

Range ambiguities become more pronounced at higher altitudes and longer slant ranges due to the overlapping of several inter-pulse periods between pulse transmission and reception. High PRF values increase range ambiguities, due to the overlapping of received pulses in time. By imposing an upper bound to the PRF, range ambiguities from the main lobes of successive pulses can be avoided. This PRF upper bound is given by Equation 2.26 [32]

$$PRF < \frac{c_0 D_{el}}{2\lambda R \tan\eta} \tag{2.26}$$

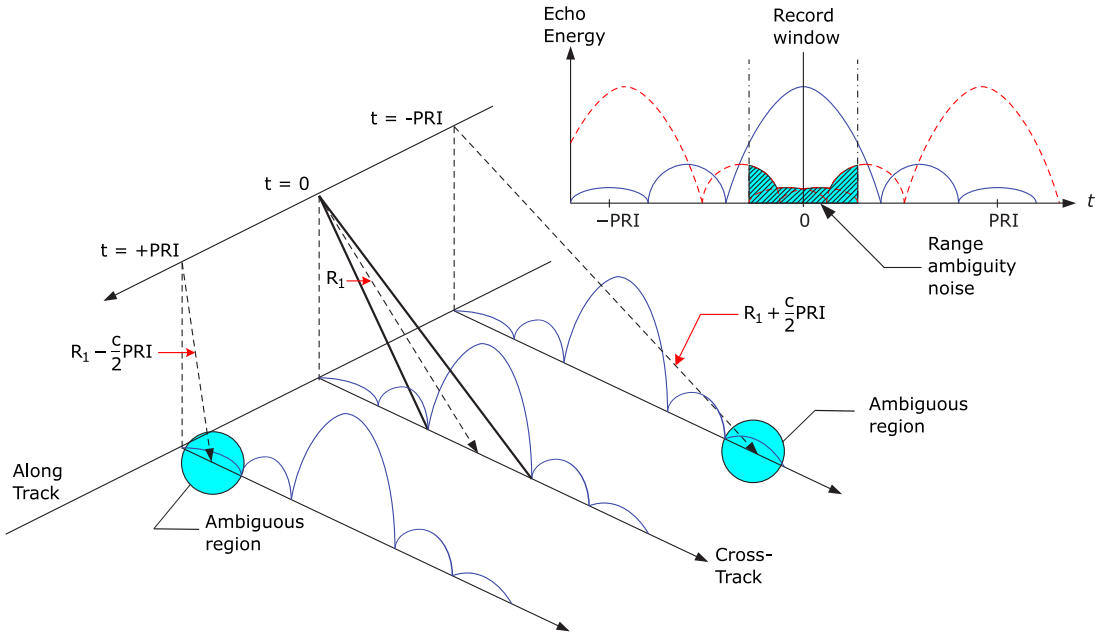

Figure 2.6: Timing diagram for the transmitted pulses along the range direction for three consecutive PRIs. The record window is shown with ambiguous signals overlapping with the desired signal return. Image adapted from [32, p. 297].

D_{el} is the antenna dimension in elevation.

2.7 Azimuth-Ambiguity-to-Signal Ratio

Similar to range ambiguities, azimuth ambiguities appear as the duplication of image data along the azimuth dimension. This occurs in situations where the antenna main beam coincides with an area of low reflectivity, but the sidelobes coincide with objects of high reflectivity. These sidelobe returns are strong enough to appear in the image formed by the SAR processor. Figure 2.7 depicts a harbour scene imaged by the USSR Almaz-1 where multiple "duplicates" occur along the azimuth dimension. High-reflectivity objects on the harbour front got superimposed on the low-reflectivity water surface returns. These duplicates decreased in intensity as the SAR platform propagated along its orbit and the sidelobe levels got smaller. Figure 2.8 shows another example of azimuth ambiguities. The Canadian RADARSAT-2 imaged high-reflectivity offshore structures, which caused duplicate distortions in the imaged scene.

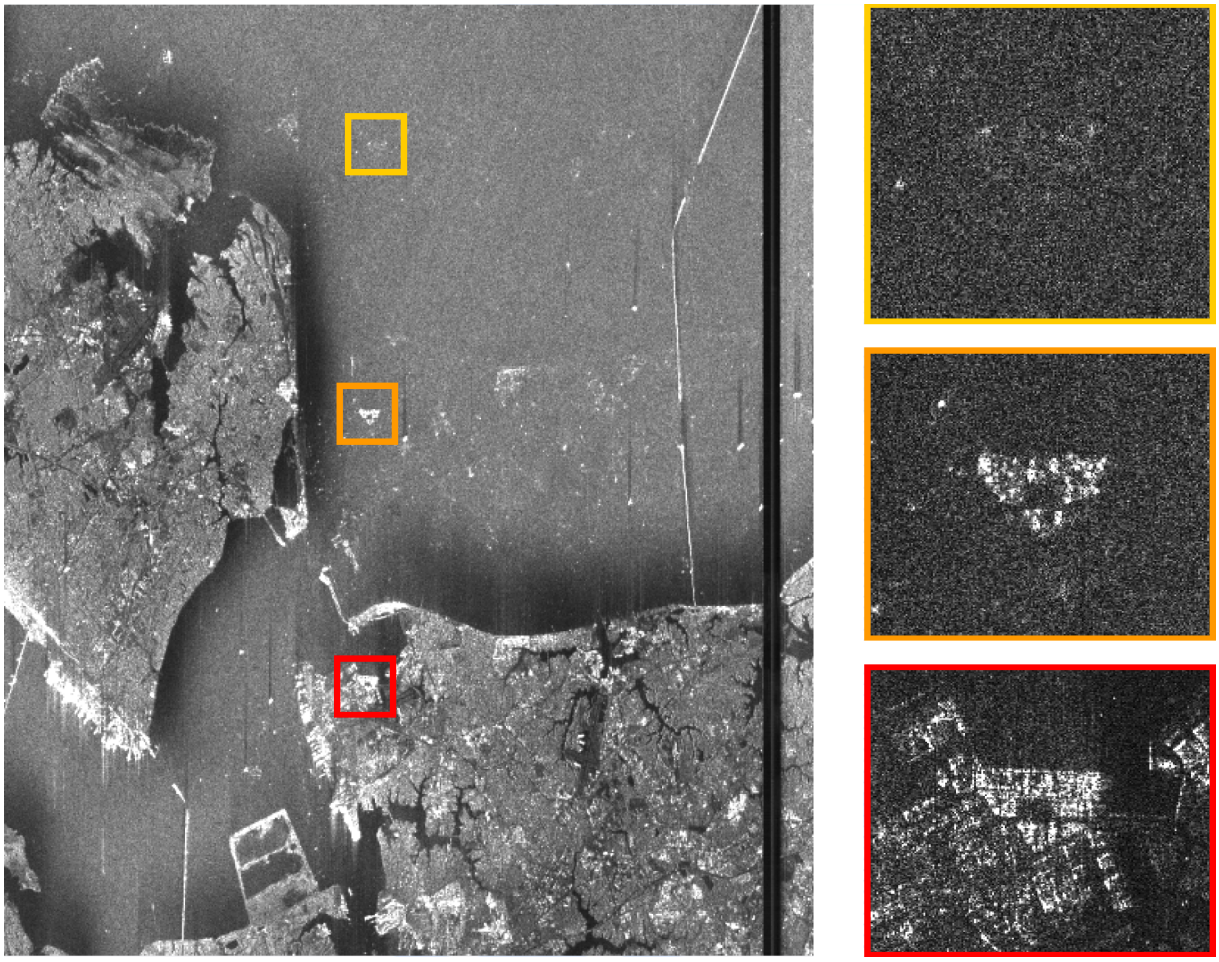

Figure 2.7: Azimuth ambiguities present in imaged scene from Almaz-1 SAR sensor. Orbit 2365A over Norfolk, USA. The area in the red square represents an area of high reflectivity, which has a first duplicate shown in the orange square and a second duplicate in the yellow square. Image obtained from [33].

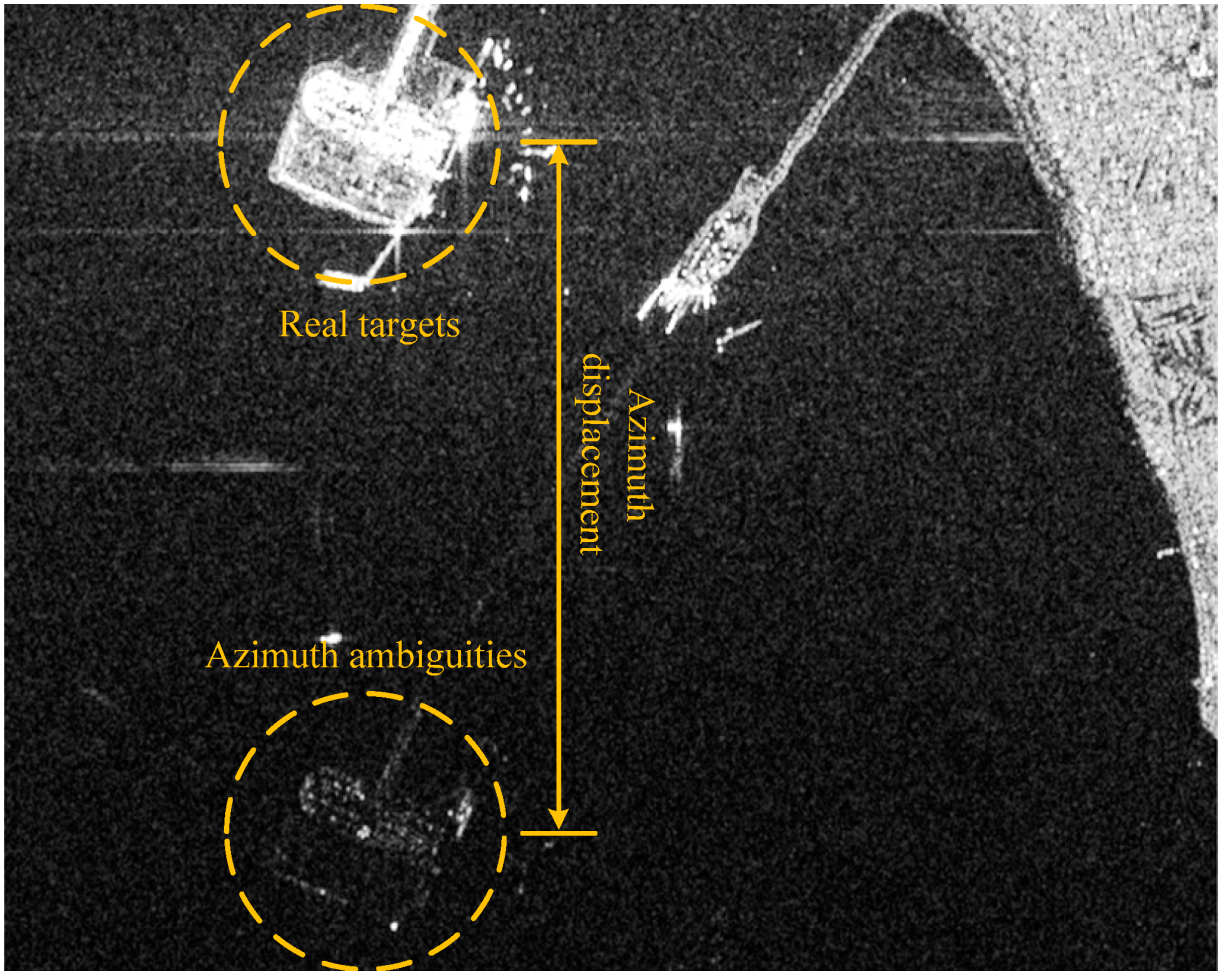

Figure 2.8: SAR Azimuth ambiguities over Roberts Bank Port at Georgia Strait, Vancouver. Acquired by RADARSAT-2. High-reflectivity offshore structures cause duplication over low-reflectivety scene. Image obtained from [34].

The AASR is an ambiguity measurement arising from the finite sampling of the Doppler spectrum at integer intervals of the PRF [32]. Due to this finite sampling of the Doppler spectrum, the Doppler frequency components outside the sampling frequency interval $-PRF/2 \leq B_D < PRF/2$ are aliased into the main processed Doppler frequency range, distorting the desired signal return.

Figure 2.9 illustrates the azimuth ambiguity timing diagram, with spectral components outside the sampled frequency interval folded back into the main part of the spectrum.

The mathematical expression for the AASR is given by Equation 2.27 [18], [32] with Doppler frequency, f_D, processed azimuth bandwidth, B_γ, the 2-way (TX/RX) azimuth antenna field pattern, $C_{2way,az}$ and N_A representing the number of ambiguities considered in the calculation.

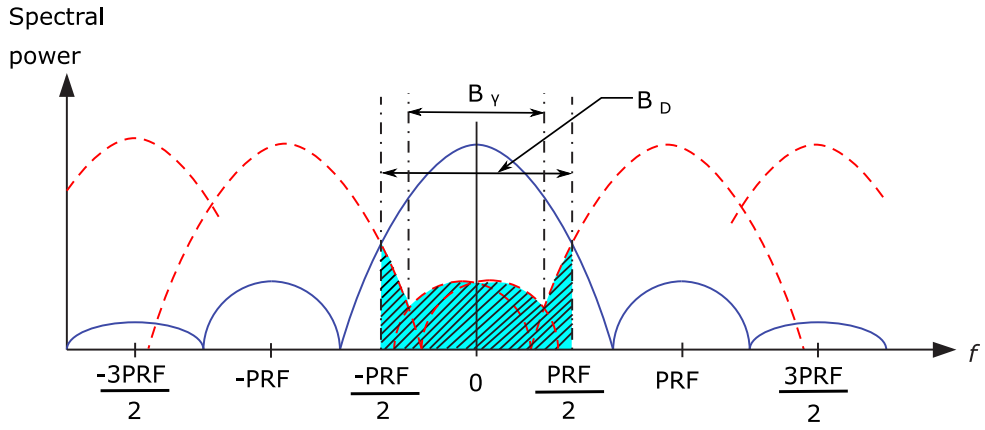

Figure 2.9: SAR azimuth ambiguity timing diagram for PRF $= B_D$. Spectral components outside the sampled frequency interval folded back into the main part of the spectrum. Image adapted from [32, p. 297].

$$AASR = \frac{\sum_{\substack{m=-N_A \\ m\neq 0}}^{N_A} \int_{-B_\gamma/2}^{B_\gamma/2} \mid C_{2way,az}(f_D + m \cdot PRF) \mid^2 df}{\int_{-B_\gamma/2}^{B_\gamma/2} \mid C_{2way,az}(f_D) \mid^2 df} \tag{2.27}$$

The relationship between Doppler frequency and azimuth angle, ϕ_{az}, given by Equation 2.28, is used to express the azimuth antenna patterns in terms of Doppler frequency.

$$f_D = \frac{2V \sin \phi_{az}}{\lambda} \tag{2.28}$$

Typical values specified for the AASR in SAR systems are in the order of $-20\ dB$ [18], [26], [32]. This value is based on the assumptions of: uniform target reflectivity throughout the imaged scene, negligible coupling between azimuth and range ambiguities, no distortion to the antenna pattern at different elevation angles.

Azimuth ambiguities are more prevalent in high resolution SAR imaging [32], [35], where high reflectivity targets appear in a low reflectivity scene, with sidelobe signal returns stronger than those from the the main lobe, causing ghost targets in the image.

Azimuth ambiguities are largely mitigated by proper design of the SAR antenna and tapering in azimuth, and proper PRF selection. Low values of PRF increase azimuth ambiguities due to spectral aliasing. Azimuth ambiguities are also suppressed by reducing the processed azimuth bandwidth, but this in turn worsens the radar's azimuth spatial resolution.

The ambiguities are displaced from the target signal in azimuth, with the displacement, Δ_{az}, given by Equation 2.29 [35]

$$\Delta_{az} = \frac{\lambda(f)PRF}{2V\sqrt{1-\left(\frac{\lambda(f)PRF}{2V}\right)^2}} \cdot \frac{H_{orb}}{\cos\eta} \tag{2.29}$$

η is the incidence angle and $\lambda(f)$ is the radar wavelength between $f_c - B_p/2 \leq f \leq f_c + B_p/2$. f_c is the radar centre frequency and B_p is the transmitted pulse bandwidth.

2.8 PRF Constraints

The constraints imposed on the PRF selection by system parameters - antenna length, altitude, imaged swath width, pulse length and incidence angle ranges - are collated into the minimum and maximum values for PRF. These together with the PRF blind ranges due to the transmit events and nadir echo returns are established in this section.

From literature, the design of an acquisition geometry and PRF selection are usually based on a timing-diagram analysis. Figure 2.10 illustrates a typical timing-diagram complete with PRF blind ranges, nadir echo returns and the minimum and maximum PRF values for unambiguous imaging of the intended scene. The goal with such a timing-diagram would be to maximise the swath width of the intended imaging scene, while avoiding eclipsing of the radar receiver. In Figure 2.10 the valid PRF values at specific look angles are indicated by the empty white regions. The following sections describe each of these constraints and how they influence the choice of an appropriate PRF.

2.8.1 PRF Minimum and Maximum

For a spaceborne SAR in a circular orbit, the minimum PRF, PRF_{min}, given by Equation 2.30, should exceed the Doppler bandwidth of the imaged scene and is determined by the platform altitude and the antenna azimuth length [36], [37].

$$PRF_{min} = \frac{2V}{D_{az}} = \frac{2}{D_{az}}\sqrt{\frac{\mu}{R_E + H_{orb}}} \tag{2.30}$$

It is noted that the PRF_{min} is independent of the transmitted signal frequency. The maximum PRF, PRF_{max}, is a derived with the aim of mitigating range ambiguities. Given by Equation 2.31, it must be less than the inter-pulse period and is determined from the transmit pulse length, τ_p, the transmitter timing margin, τ_m and the scene duration, τ_w [36], [37]

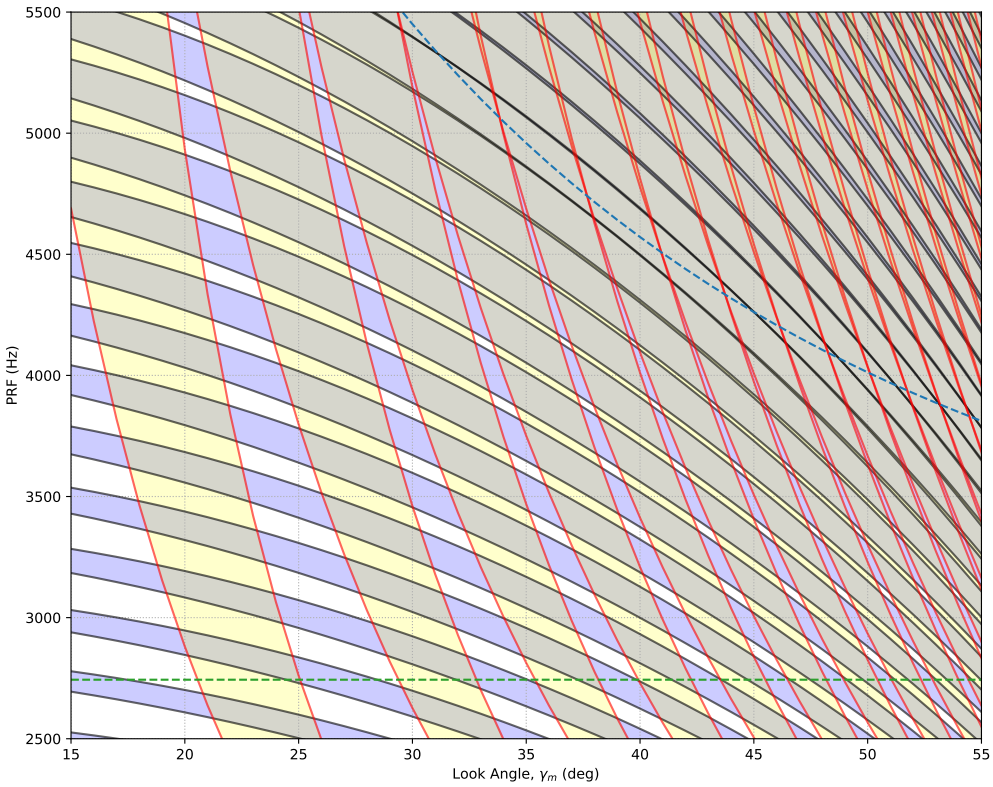

Figure 2.10: Typical imaging geometry timing-diagram illustrating the minimum PRF (green dashed) and maximum PRF (blue dashed) values together with the PRF blind ranges (blue regions) and nadir echo returns (yellow regions). White regions indicate valid imaging scenarios.

$$PRF_{max} = \frac{1}{2\tau_p + \tau_w + \tau_m} \tag{2.31}$$

$\tau_w = 2W_r / c_0$. $W_r = R_f - R_n$ is the slant range swath width between the nearest range of the swath, R_n and the farthest range of the swath, R_f. The 2-way propagation delay for these slant ranges are given by:

$$\tau_n = \frac{2R_n}{c_0} \quad \text{and} \quad \tau_f = \frac{2R_f}{c_0}$$

From Equation 2.30 and Equation 2.31 is should be clear that for a given antenna azimuth length and platform altitude, PRF_{min} would be constant over all look angles as shown in Figure 2.10, but PRF_{max} would vary as the imaging swath varies with look angles.

2.8.2 PRF Blind Ranges

Due to the nature of pulsed radars, not all PRF values between the minimum and maximum are available for use on SAR platforms. To avoid receiver saturation, the receiver is switched off during pulse transmission events. Therefore the SAR receiver is effectively blind, or "eclipsed", during these intervals. Unlike conventional radar systems where the blind ranges stay constant over range, in a side-looking SAR system imaging a spherical geometry, these blind ranges vary over distance and are dependent on the transmitter pulse length and margin, as well as the imaged scene itself. To avoid these blind ranges, the PRF must satisfy the inequality in Equation 2.32 [36], [37], with $N \in \{1, 2, 3, ...\}$.

$$\frac{N-1}{\tau_n - (\tau_m/2) - \tau_p} < PRF < \frac{N}{\tau_f + \tau_p + (\tau_m/2)} \tag{2.32}$$

In Figure 2.10 the PRF blind ranges are indicated as the curved blue regions. These regions vary with look angle, broadening as PRF increases and squeezing together at larger look angles.

2.8.3 Nadir Echo Returns

The antenna sidelobes radiate energy when imaging, and therefore the SAR's nadir point is also illuminated and generate return echoes. These echo returns, τ_{nadir}, depend on the SAR platform altitude as given by Equation 2.33, and create ambiguities similar to range ambiguities where different pulse returns are superimposed over each other at the receiver.

$$\tau_{nadir} = \frac{2H_{orb}}{c_0} \tag{2.33}$$

The nadir echo return duration depends on the characteristics of the imaged terrain [32], but is at least as long as the transmitter pulse length, τ_p [38].

Figures 2.11 and 2.12 were taken by the TerraSAR-X mission and show the presence of strong nadir returns. These cause high signal level distortions across the image scene along the flight direction.

To avoid interference from these nadir returns, the PRF must satisfy the inequality in Equation 2.34 [36], [37], with $M \in \{1, 2, 3, ...\}$. These nadir eclipse regions are dependent on the transmitter pulse and margin, the nadir propagation delay as well as the imaged scene itself.

$$\frac{M-1}{\tau_n - (\tau_m/2) - \tau_p - \tau_{nadir}} < PRF < \frac{M}{\tau_f + \tau_p + (\tau_m/2) - \tau_{nadir}} \tag{2.34}$$

In Figure 2.10 the nadir echo returns are indicated as yellow regions.

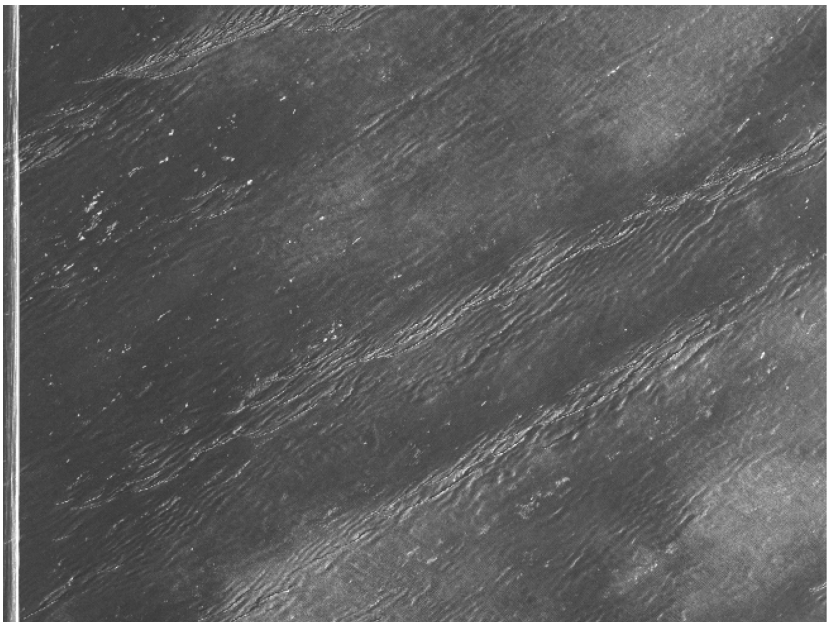

Figure 2.11: TerraSAR-X SAR image with strong nadir return taken over Mali in a descending orbit using a right-looking geometry with the flight direction along the vertical axis of the image and the range direction along the horizontal axis. A strong nadir echo can be seen as a bright vertical line on the left edge of the image parallel to the flight direction of the SAR platform. Image obtained from [39].

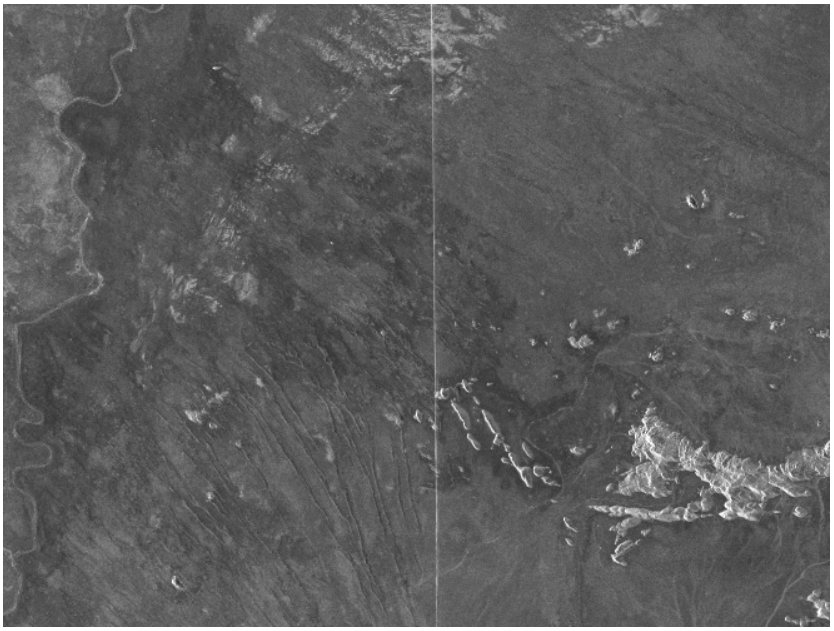

Figure 2.12: TerraSAR-X SAR taken over Australia in an ascending orbit using a right-looking geometry with the azimuth direction along the vertical axis. Here the nadir echo can be clearly seen as a bright vertical line through the centre of the images. Image obtained from [40].

2.9 Summary

This chapter presented an overview of the fundamental principles of spaceborne SAR imaging geometries. The different performance metrics for designing a SAR system were established, and were utilised in later chapters for the comparison between AESA and reflector systems. These performance metrics included the definitions for range and azimuth resolution, signal-to-noise ratio, clutter-to-noise ratio and noise-equivalent sigma zero. The chapter also covered the different types of ambiguities which might arise in SAR imaging sessions and ways in which they can be mitigated. The expressions for measuring the losses induced by these ambiguities in both the azimuth and range dimensions were established. The limitations imposed on the choice of PRF by the different system parameters - antenna length, platform altitude, swath width, transmitter pulse length and incidence angle - were covered by the PRF_{min} and PRF_{max} values. These constraints were visualised with the aid of a timing-diagram, typically used for analysis and design of an imaging acquisition geometry. These, together with the PRF blind ranges and the eclipsing of the SAR receiver by strong nadir returns were used in Chapter 3 to verify our software models, and in Chapter 4 during the system design phases.

3 Verification of Models

As with any software engineering project, the libraries, modules and code within the notebooks needed to be verified and tested against known systems and results.

This chapter serves to verify the software modules by modelling systems from literature and comparing the obtained results against published results. Verification for the planar array system was done for a narrow swath scenario using the conceptual array specified in [18, pp. 6–8], and for a wide swath scenario using RADARSAT-2 parameters. Verification of the reflector system was done using the conceptual reflector system specified in [18, pp. 8–12].

The Python kernel was chosen for the coding language allowing for the creation of software modules which can either be included in the Jupyter notebook or used as stand-alone libraries. For the most part, all generic code was separated out into individual Python classes and modules. These include classes for the different antenna aperture configurations, i.e. *Rectangular, Circular, Linear Array* and *Planar Array*. Modules were created for the different performance metrics, i.e. *AASR, RASR* and *NESZ*. The Earth model and all geometry related calculations are described in the *Spherical Earth Model* module, and PRF-related calculations such as blind ranges and nadir echoes are described in the *Prf* module.

Individual Jupyter notebooks were created to model specific system designs and to serve as rapid system verification tools. The results from these notebooks, including data sets and visualisations were easily exported to various formats thanks to libraries available on the large open-source Python community.

Since the choice of PRF is coupled to a number of system parameters, including the SAR platform's orbital altitude, antenna azimuth length, transmitter pulse length (or duty cycle), ground swath coverage, incidence angle, look angles and ambiguity performance, it was verified first. Verification was done according to the constraints detailed in section 2.8 to ensure that the PRF, together with the relevant system parameters, do not coincide with transmission events or nadir echo returns, which would cause eclipsing of the radar receiver. The libraries and modules used for the PRF verification are listed in Appendix A. The software module for the PRF constraints were verified by modelling individual system parameters - antenna azimuth length, SAR platform altitude, transmitter pulse length, ground swath width, incidence angle ranges and look angle ranges - over a range of values. In each case the chosen system PRF should have fallen outside eclipsed regions.

The verification of the 3 dB NESZ performance, described in section 2.5, over the desired range of incidence angles followed next. Modelling and verification was done using the antenna patterns, without tapering, instead of a more in-depth field distribution model. The same was done for the verification of RASR and AASR performance, as described in section 2.6 and section 2.7 respectively.

The libraries and modules for the NESZ, AASR and RASR verification are listed in Appendix A.

3.1 Planar Array Model

The planar array model was compared against two systems: The conceptual planar array model described in [18, pp. 6–8] and RADARSAT-2 in the *Wide Fine* operational mode. The first makes use of a narrow swath imaging mode at C-band with high spatial resolution. The second scenario models a wide swath high resolution imaging mode using 3 beams on TX, with a single RX beam steered across the entire swath as the pulse travels along the ground.

3.1.1 Narrow Swath Scenario

A single TX beam was modelled to cover the entire swath, and a narrower RX beam was modelled to steer in elevation over the entire swath on reception. No azimuth beamsteering was performed. The system parameters obtained from [18, pp. 6–8] are presented in Table 3.1 and the performance parameters were evaluated over the look angle range of 28.8° to 36.1° corresponding to an incidence angle range of 32.1° to 40.6°.

Table 3.1: Narrow swath planar array system parameters obtained from [18, pp. 6–8].

Parameter	Value	Parameter	Value
Operating Frequency	5.4 GHz	Receive Antenna height	2 m
Orbital Altitude	650 km	Antenna Mounting Angle	32.45 $^\circ$
Average Transmitter Power	300 W	Swath Width	$\geq$ 125 km
Transmitter Duty Cycle	8 %	Resolution (rg, az)	$\leq$ 6 m $\times$ 6 m
PRF	1610 Hz	Processed Azimuth Bandwidth	1150 Hz
Noise Figure	3.6 dB	NESZ	$<$ -25 dB
Losses	3 dB	RASR	$<$ -20 dB
Antenna length	10 m	AASR	$<$ -20 dB
Transmit Antenna Height	0.4 m		

Figure 3.1 shows the results of the PRF verification step with the details in the figure caption. The choice of PRF was compared against (a) radar altitude, (b) antenna azimuth length, (c) TX pulse length, (d) swath width, (e) incidence angle and (f) look angle, with all system parameters listed in Table 3.1. The PRF limits were obtained using Equation 2.30 to Equation 2.34. The choice of system parameters - antenna azimuth length, SAR platform altitude, transmitter pulse length, swath width and incidence angle ranges - were derived during the initial design phase in [18]. For example,

the antenna length should not be longer than twice the required single-look azimuth resolution [36], with the TX pulse length and PRF as large as possible to minimise the required peak transmitter power. Users tend to require the largest possible swath widths with specified resolution and sensitivity (NESZ) requirements. Incidence angle, and accordingly look angle, is strongly related to the intended application and limited by the PRF constraints.

Figure 3.1 shows the PRF timing analysis done for the narrow swath (125 km) scenario. Except for the case of antenna length, the eclipsed areas have non uniform responses over the different parameter ranges. White regions on the graphs, between the PRF minimum and PRF maximum lines, indicate valid PRF ranges, where no eclipsing of the radar receiver occurs. The choice of a valid PRF value had to lie within these white regions for the respective system parameter values. From these graphs the choice of 1610 Hz for the PRF, indicated as a horizontal black dashed line, appears valid, with the respective system parameters indicated with vertical black dashed lines. It avoids eclipsing and oversamples the Doppler bandwidth of the scene by a factor of 1610/1507 or 1.07, thus satisfying the requirement of Equation 2.8.

Figure 3.2 illustrates the 3 dB NESZ values for the stripmap mode calculated using Equation 2.20. Each individual red graph illustrates the NESZ over the narrow receive beam swath. This narrow receive beam is scanned along the swath illuminated by the wider transmit beam. The green graph indicates the effective NESZ over the entire swath. The step size between the receive beams was arbitrarily chosen for simulation purposes, but for a real system would be dependent on the capability of the digital phase shifters. The required NESZ of -25 dB was specified as a system requirement in [18].

Figure 3.3 shows results published in [18, p. 8] for the planar array NESZ over the same 125 km swath in stripmap mode. The calculated results for NESZ in Figure 3.2 show similar behaviour of increasing at higher incidence angles as shown in Figure 3.3, corresponding to farther slant ranges, and the 3 dB RX beamwidth increasing as the beam is steered away from boresight (32.45°).

The slight mismatch of approximately 2 dB between calculated values and those published by [18] are attributed to modelling of the antenna patterns. No exact mathematical models for the antenna patterns were presented in [18]. For Figure 3.2 an uniformly illuminated aperture was assumed without any tapering applied with the radiating elements in elevation spaced $d = \lambda/2$ apart. If an antenna taper were applied, the gain and NESZ would decrease slightly.

The published results in [18] were limited to figures, with no exact values specified. Therefore, based on the comparison between Figure 3.2 and Figure 3.3 this verification step was successful.

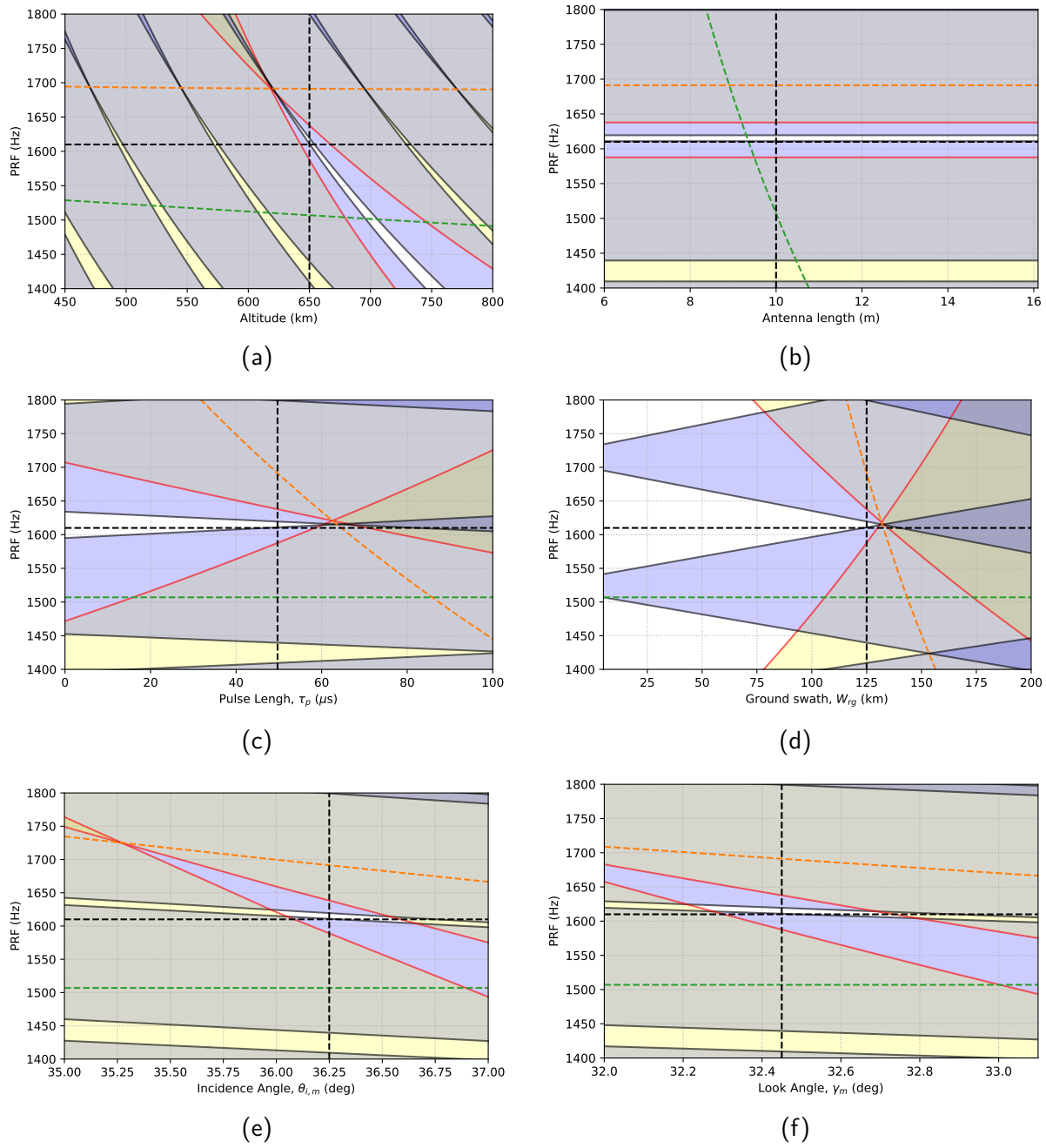

Figure 3.1: Narrow swath PRF analysis. PRF blind ranges due to transmitter pulse eclipsing are indicated as blue areas between solid black lines, whereas blind ranges due to nadir echo returns are indicated as yellow areas between solid red lines. Valid PRF values are the white spaces between the minimum (green) and maximum (orange) PRF limits. (a) Compares the PRF vs radar altitude. The minimum and maximum PRF decreases with increasing altitude. (b) Compares PRF vs antenna length. PRF maximum is 1691 Hz and PRF minimum decreases with antenna length and is 1507 Hz for a 10 m antenna. (c) Compares PRF vs TX pulse length. PRF maximum decreases with increasing pulse lengths, but PRF minimum is constant at 1507 Hz. (d) Compares PRF vs ground swath. PRF maximum decreases with increasing swaths and PRF minimum is constant at 1507 Hz. (e) Compares PRF vs incidence angle. The PRF is less constrained at smaller incidence angles, with no usable PRFs at incidence angles much larger than 70°. PRF minimum is constant at 1507 Hz, but PRF maximum decreases with increasing incidence angles. (f) Similar to (e), smaller look angles constrain the choice of PRF less with large look angles being less useful. PRF minimum is constant at 1507 Hz and PRF maximum decreases with increasing look angles.

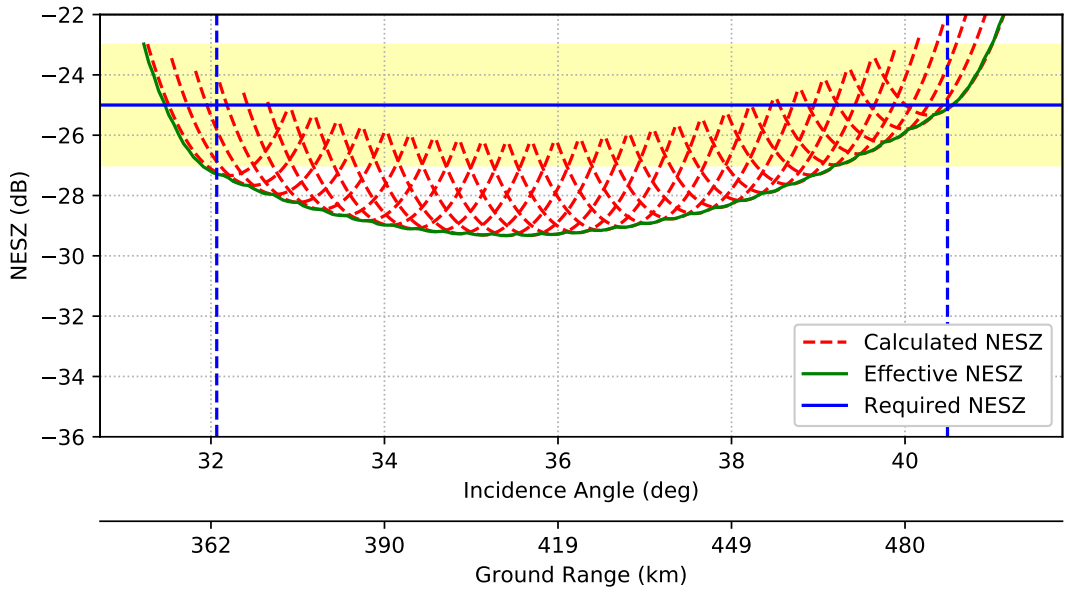

Figure 3.2: Calculated narrow-swath NESZ vs incidence angle for planar array modelled with the system parameters specified in [18, pp. 6–8] over the incidence angle range 32.1° to 40.6°. The required NESZ value is indicated as a solid horizontal blue line, with the calculated NESZ values indicated in red. The effective NESZ values as the RX beam scans over the swath are indicated in green. The incidence angles of interest are indicated between the two dashed vertical blue lines.

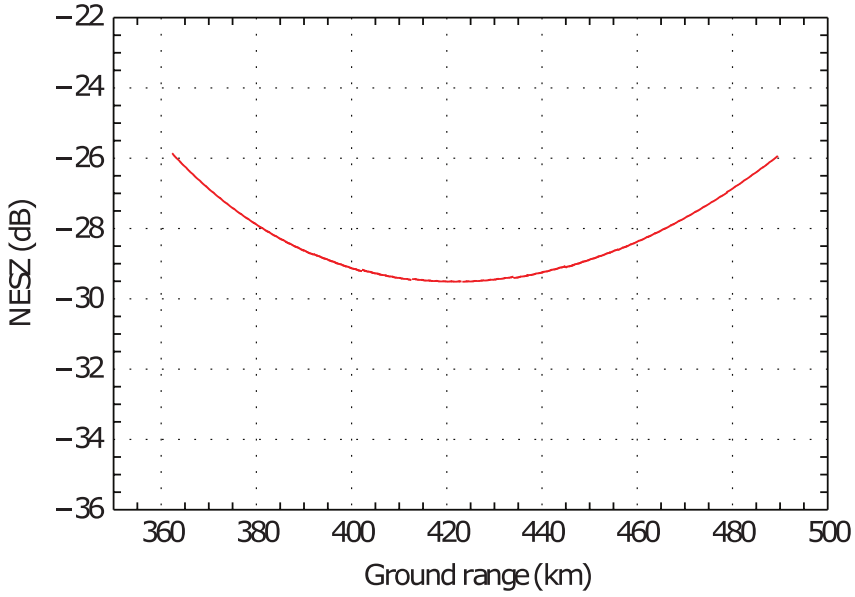

Figure 3.3: Planar array NESZ vs ground range depicted in [18, p. 8]. This is compared against the calculated values shown in Figure 3.2.

Figure 3.4 illustrates in red the AASR value calculated from the processed azimuth bandwidth obtained from the orbital velocity, 1255.79 Hz, and from the reduced bandwidth, 1150 Hz, specified in [18] in orange. These values were calculated using Equation 2.27. From [18] the processed azimuth bandwidth was reduced, at the expense of worsened azimuth resolution, to improve the AASR performance. For the original bandwidth of 1255.79 Hz the AASR was -20.1 dB, which only marginally met the -20 dB requirement. The reduced bandwidth AASR value was approximately -22 dB.

Figure 3.5 shows results published in [18, p. 8] for the planar array AASR over a 125 km swath in stripmap mode. The slight value mismatch of approximately 1 dB can be attributed to the differences in Earth models used for calculating the orbital velocity and the modelling of the antenna pattern. No tapering in azimuth was applied to the antenna pattern, so the higher sidelobes would definitely have a stronger impact on the ambiguity performance. With an antenna taper applied, the azimuth ambiguity performance would improve.

The published results in [18] were limited to figures, with no exact values specified. Therefore, based on the comparison between Figure 3.4 and Figure 3.5 this verification step was successful.

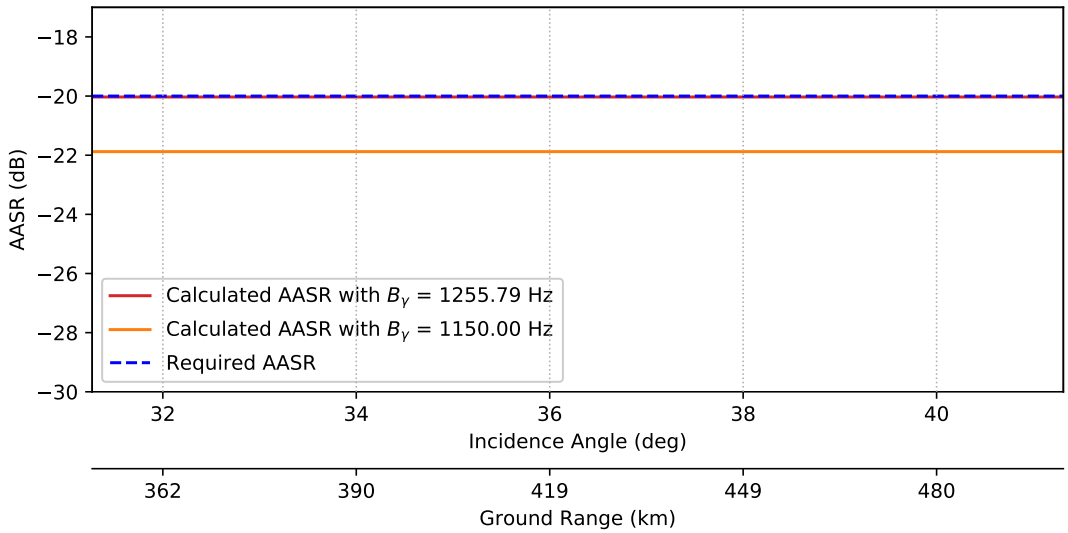

Figure 3.4: Calculated narrow-swath AASR vs incidence angle for the planar array modelled with the system parameters specified in [18, pp. 6–8]. The required AASR value is indicated as a dashed horizontal blue line, with the calculated AASR value using a processed azimuth bandwidth of 1255.8 Hz indicated in red. The calculated AASR with the processed azimuth bandwidth reduced to 1150 Hz is indicated in orange.

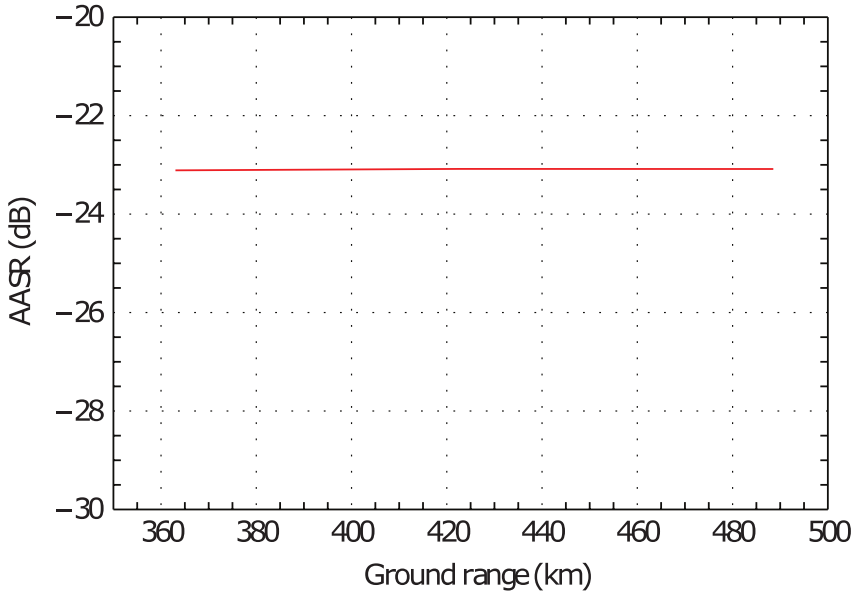

Figure 3.5: Planar array AASR vs ground range depicted in[18, p. 8]. This is compared against the calculated values shown in Figure 3.4.

Figure 3.6 illustrates the calculated RASR values and can be seen to be below the required -20 dB level over the observed incidence angle range. These values were calculated using Equation 2.25. The overall shape of the RASR response is similar to that of Figure 3.7, with the differences attributed to possible mismatches in antenna pattern models. No mathematical models were specified in [18] for the antenna patterns, therefore an uniformly illuminated aperture was assumed without any tapering applied.

Figure 3.7 shows the results published in [18, p. 8] for the planar array. The antenna pattern shape and tapering in elevation plays an important role in determining the values of the RASR. By suppressing the sidelobes in elevation, the RASR performance can be improved further.

The published results in [18] were limited to figures, with no exact values specified. Therefore, based on the comparison between Figure 3.6 and Figure 3.7 this verification step was successful.

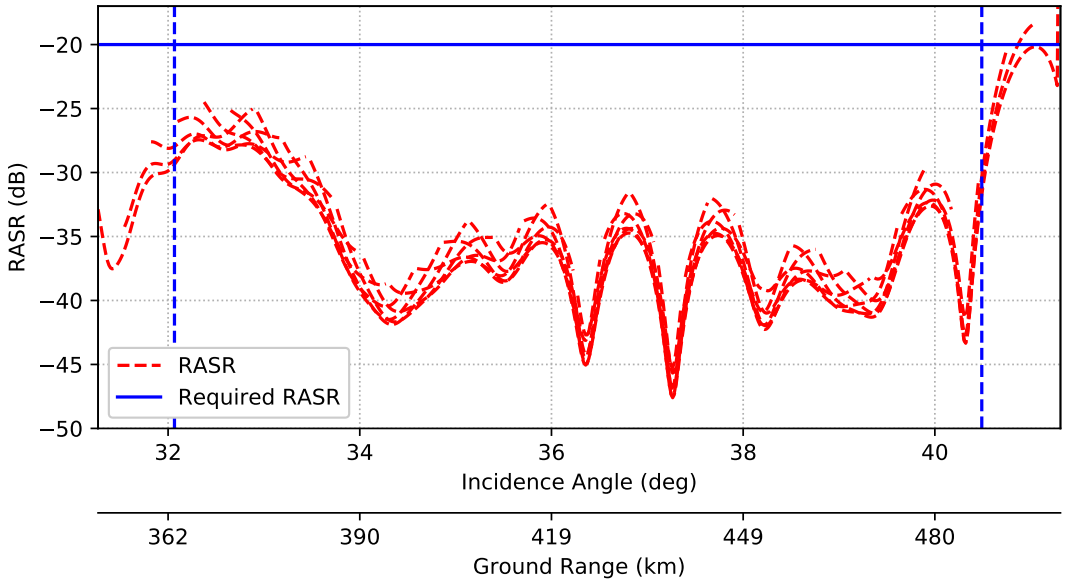

Figure 3.6: Calculated narrow-swath RASR vs incidence angle for the planar array modelled with the system parameters specified in [18, pp. 6–8]. The required RASR value is indicated as a solid horizontal blue line, with the calculated RASR values in red. The incidence angles of interest are indicated between the two dashed vertical blue lines.

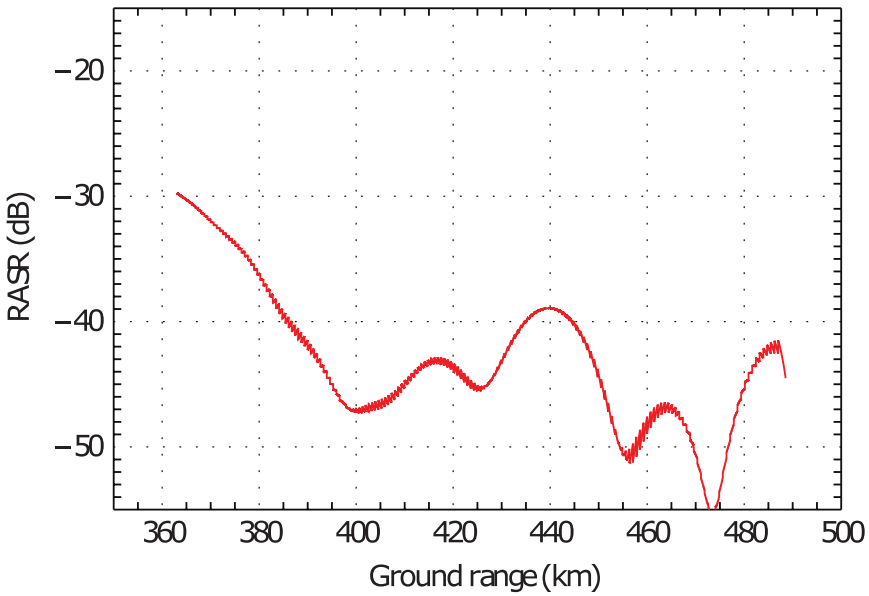

Figure 3.7: Planar array RASR vs ground range depicted in [18, p. 8]. This is compared against the calculated values shown in Figure 3.6.

3.1.2 Wide Swath Scenario

For a secondary verification, the RADARSAT-2 *Wide Fine* mode is modelled using three separate beams (F0W1, F0W2 and F0W3) to illuminate a wide swath at high spatial resolution over the incidence angle range of 20° to 45°. The three transmission beams have different characteristics in elevation in terms of beamwidth, number of active elements, gain, steering direction and ground swath coverage. Table 3.2 lists the system parameters and requirements while Table 3.3 list the parameters for the 3 transmission beams.

Table 3.2: Wide swath RADARSAT-2 system parameters [26], [27].

Parameter	Value	Parameter	Value
Operating Frequency	5.405 GHz	Antenna Mounting Angle	29.8°
Orbital Altitude	798 km	Elevation Elements	32
Peak Transmitter Power	1650 W	Azimuth Elements	16
Pulse length	21 μs	Processed Azimuth Bandwidth	900 Hz
PRF	2600 Hz	Spatial Resolution (rg x az)	5.2 m $\times$ 7.7 m
Noise Figure	4.3 dB	Chirp Bandwidth	30 MHz
Losses	4.1 dB	NESZ	$<$ -24 $\pm$ 2 dB
Antenna length	15 m	AASR	$<$ -20 dB
Antenna height	1.37 m	RASR	$<$ -20 dB

Table 3.3: RADARSAT-2 Wide Fine mode beam configuration [26], [27].

Parameter	Near Beam F0W1	Middle Beam F0W2	Far Beam F0W3
Azimuth Elements	16	16	16
Azimuth Beamwidth	0.19°	0.19°	0.19°
Elevation Elements	6	9	13
Elevation Beamwidth	10.99°	7.33°	5.07°
TX Gain	41.4 dBi	43.2 dBi	44.8 dBi
Ground Swath	174.0 km	141.2 km	122.3 km

The three TX beams each illuminates a wide sub-swath, and a fine (narrow) RX beam is scanned across the different sub-swaths to follow the pulse along the ground. This mode of operation resulted in lower NESZ and RASR performance, due to the lower gain on transmission. Either the swath width during stripmap mode needs to be shortened or the resolution needs to drop to accommodate such a wide swath.

Figure 3.8 shows the results of the PRF verification step for the wide swath scenario, with the caption detailing the results. Similar to Figure 3.1, the choice of PRF is compared against (a) radar altitude, (b) antenna azimuth length, (c) TX pulse length, (d) swath width, (e) incidence angle and (f) look angle, with other fixed parameters listed in Tables 3.2 and 3.3. The PRF limits were obtained using Equation 2.30 to Equation 2.34. Within each of these figures the chosen PRF, indicated as a horizontal black dashed line, had to fall within the white regions where no PRF blind ranges or nadir echo returns occurred. From these graphs the choice of 2600 Hz for the PRF appears valid. It avoids eclipsing and oversamples the Doppler bandwidth of the scene by a factor of 2600/994 or 2.62, thus satisfying Equation 2.8.

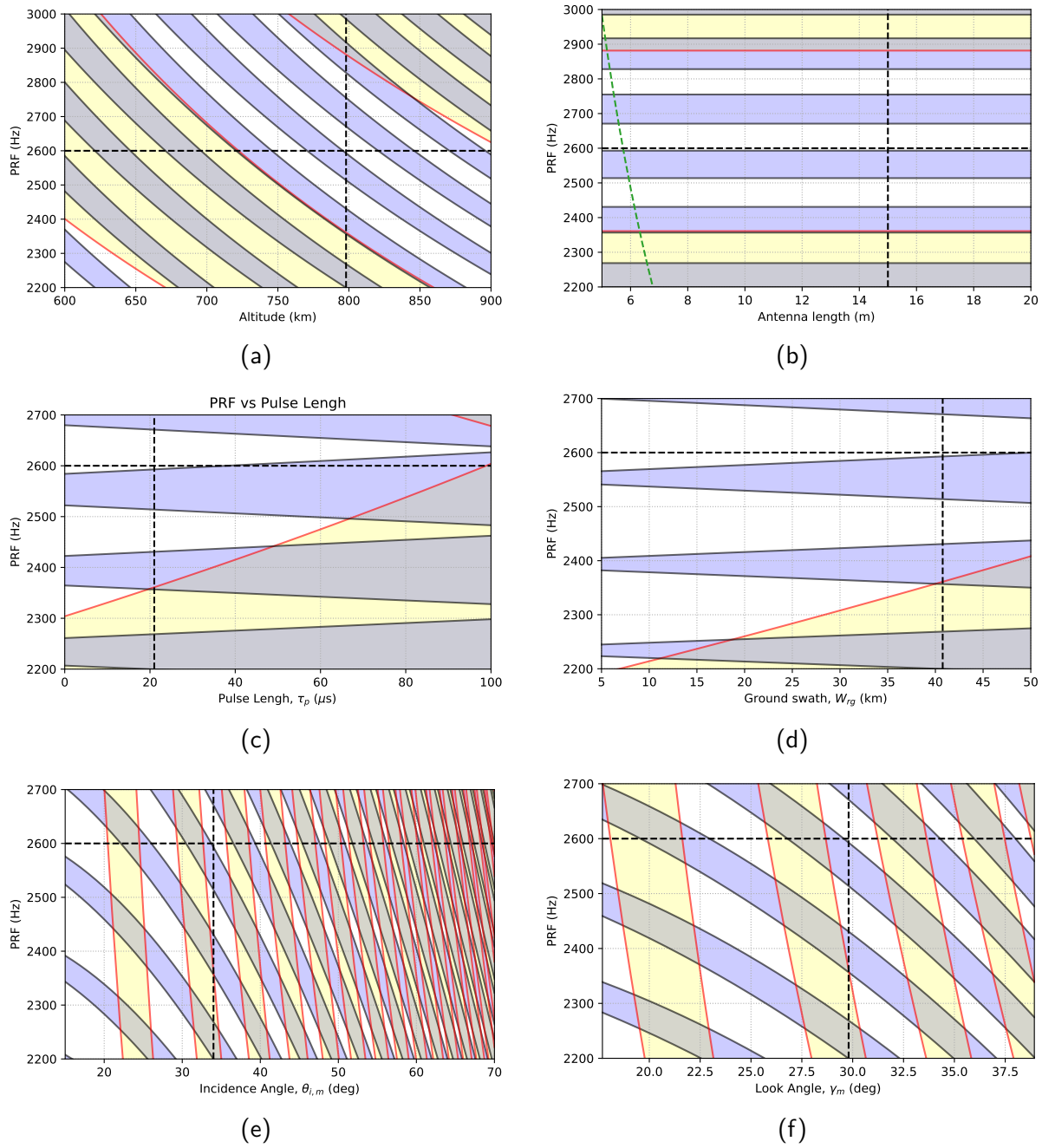

Figure 3.8: Wide swath PRF analysis. PRF blind ranges due to transmitter pulse eclipsing are indicated as blue areas between solid black lines, whereas blind ranges due to nadir echo returns are indicated as yellow areas between solid red lines. Valid PRF values are the white spaces between the minimum (green) and maximum (orange) PRF limits. (a) Compares the PRF vs radar altitude. The minimum and maximum PRF decreases with increasing altitude. (b) Compares PRF vs antenna length. PRF maximum is 5153 Hz and PRF minimum decreases with antenna length and is 994 Hz for a 15 m antenna. (c) Compares PRF vs TX pulse length. PRF maximum decreases with increasing pulse lengths, but PRF minimum is constant at 994 Hz. (d) Compares PRF vs ground swath. PRF maximum decreases with increasing swaths and PRF minimum is constant at 994 Hz. (e) Compares PRF vs incidence angle. The PRF is less constrained at smaller incidence angles, with no usable PRFs at incidence angles much larger than 70°. PRF minimum is constant at 994 Hz, but PRF maximum decreases with increasing incidence angles. (f) Similar to (e), smaller look angles constrain the choice of PRF less and large look angles being less useful. PRF minimum is constant at 994 Hz and PRF maximum decreases with increasing look angles.

Figure 3.9 illustrate the 3 dB NESZ results obtained using Equation 2.20 for the 3 beams, F0W1 in red, F0W2 in green and F0W3 in orange. Each depicts multiple graphs representing the narrow receive beam scanned across the wider transmitted sub-swaths. The calculated NESZ values were seen to attenuate at the edges, which can be attributed to the shape of the modelled TX antenna pattern. For most of the swath the NESZ values fall in or below the required -24 $\pm$ 2 dB range specified in 3.2 indicated as a solid horizontal blue line within a yellow region. To improve the NESZ performance over such a wide-swath the required resolution needs to be lowered, the transmitted power needs to be increased or the swath width has to be shortened.

No exact mathematical model for the antenna pattern was presented in [26] or {IEEEexample:radarsat2manual}, therefore a uniformly illuminated aperture with no tapering was assumed. No representation of the NESZ performance other than the -24 $\pm$ 2 dB range was specified in [26] and {IEEEexample:radarsat2manual}. Therefore, based on the calculated values in Figure 3.9, this verification step was successful.

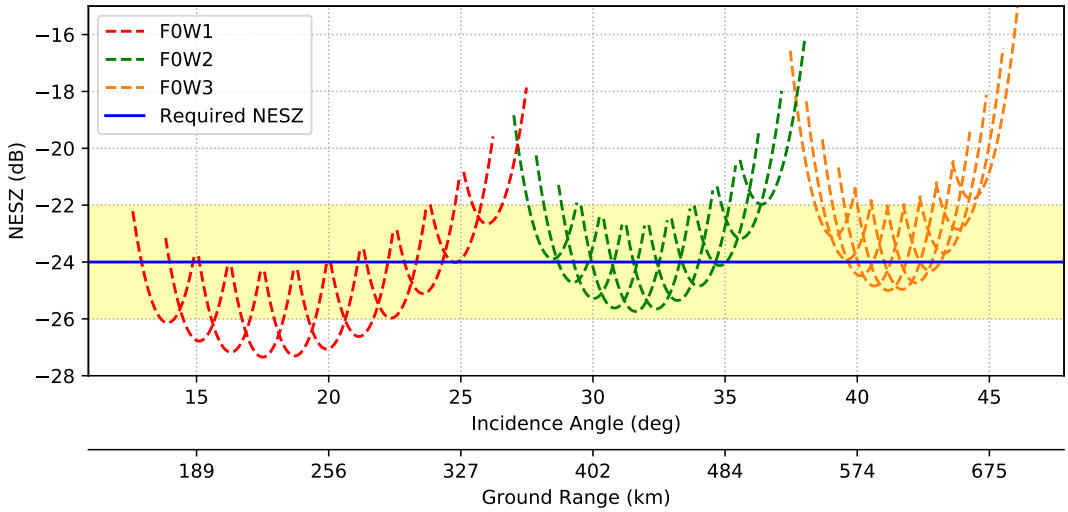

Figure 3.9: Calculated wide-swath NESZ vs incidence angle for planar array modelled with RADARSAT-2 system parameters at different look angles over the entire incidence angle range. The three curves correspond to the three transmitted beams. The required NESZ value is indicated as a solid blue horizontal line, with the ± 2 dB margin indicated in yellow.

Figures 3.10 and 3.11 illustrate the AASR and RASR values obtained when modelling the planar array with RADARSAT-2 system parameters in the *Wide Fine* mode over the incidence angle range. The AASR values are constant due to stripmap operation and below the -20 dB level over the all incidence angles. The calculated value for beam F0W1 is indicated in red, for F0W2 in green and F0W3 in orange, with the required AASR value shown as a solid horizontal blue line.

No value for the RADARSAT-2 AASR performance was obtained other than the -20 dB requirement specified in [26] and {IEEEexample:radarsat2manual}. Therefore, based on the calculated value in Figure 3.10, this verification step was successful.

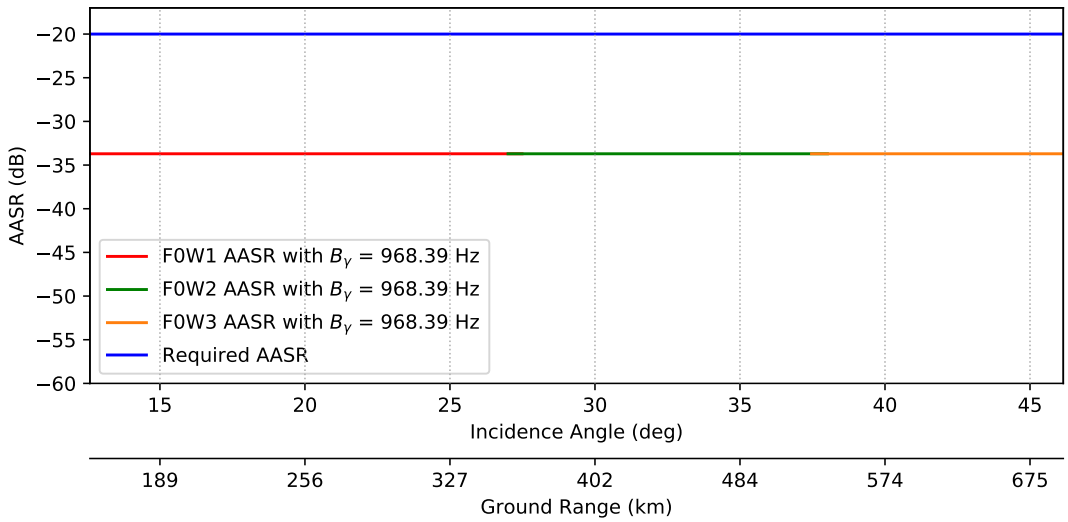

Figure 3.10: Calculated AASR vs slant range for the planar array modelled with RADARSAT-2 system parameters at the calculated processed azimuth bandwidth [26]. The required AASR value is indicated as a solid blue horizontal line, with the calculated AASR values for the three beams in red, green and orange.

The RASR values in Figure 3.11 fall below the required level only at lower incidence angles. This indicates an incorrectly modelled system parameter and can mainly be attributed to a too-wide swath during transmission. No value for the RADARSAT-2 RASR performance was obtained other than the -20 dB requirement specified in [26] and {IEEEexample:radarsat2manual}. Therefore, based on the calculated value in Figure 3.11, the TX beamwidth needs to be lowered, which will improve the TX gain, and so the RASR performance.

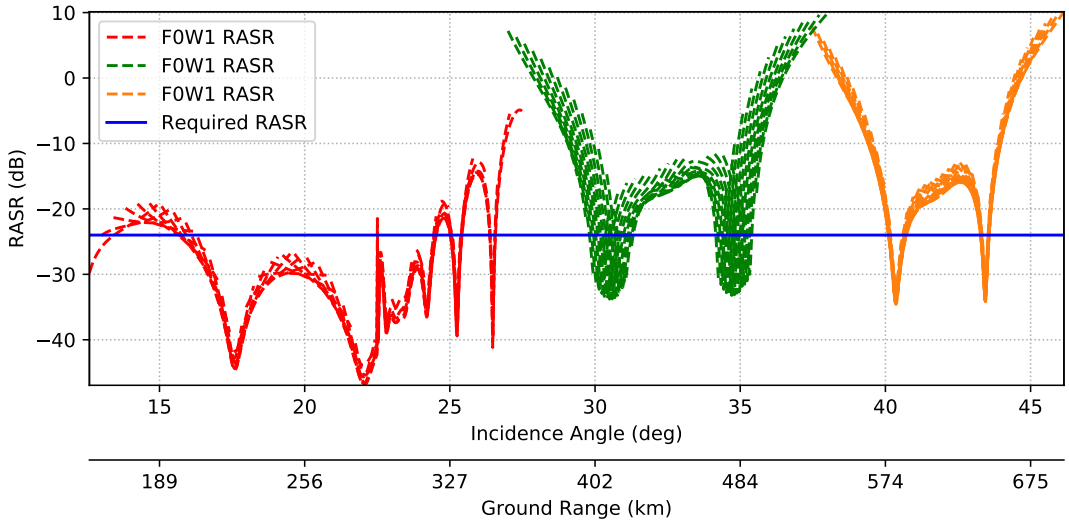

Figure 3.11: Calculated RASR vs incidence angle for the planar array modelled with RADARSAT-2 system parameters. The required RASR value is indicated as a solid blue horizontal line, with the calculated RASR values for the three beams in red, green and orange respectively.

3.2 Reflector Model

The reflector model is configured according to the conceptual reflector specifications [18, pp. 8–11] listed in Table 3.4 and the performance parameters are evaluated over the look angle range of $28.8°$ to $36.1°$. No azimuth beamforming is performed and therefore only a single channel in azimuth is used for the performance measurements.

Table 3.4: C-band reflector swath system configuration obtained from [18, pp. 8–11].

Parameter	Value	Parameter	Value
Operating Frequency	5.4 GHz	Spatial Resolution	$\leq$ 6 m $\times$ 6 m
Orbital Altitude	650 km	Processed Azimuth Bandwidth	1150 Hz
Average Transmitter Power	300 W	Antenna Diameter	10 m
Transmitter Duty Cycle	8 %	Azimuth Channels	1
PRF	1610 Hz	Elevation Channels	26
Noise Figure	3.6 dB	NESZ	$<$ -25 dB
Feed Losses	3.6 dB	AASR	$<$ -20 dB
Antenna Mounting Angle	32.45°	RASR	$<$ -20 dB
Ground Swath	$\geq$ 125 km		

Figure 3.12 illustrates that during transmission all feeds in elevation are active, illuminating a sub-

section of the reflector, resulting in a low-gain broad beam, which in turn illuminates a 125 km wide swath. Each feed illuminates a slightly overlapping angular domain in elevation [23]. In Figure 3.12 the illuminated swath during TX is shown in yellow, with different colours used to indicated the respective sub-swaths illuminated by individual feed elements. The narrow RX beam is scanned along the swath in the elevation direction by activating consecutive feed elements.

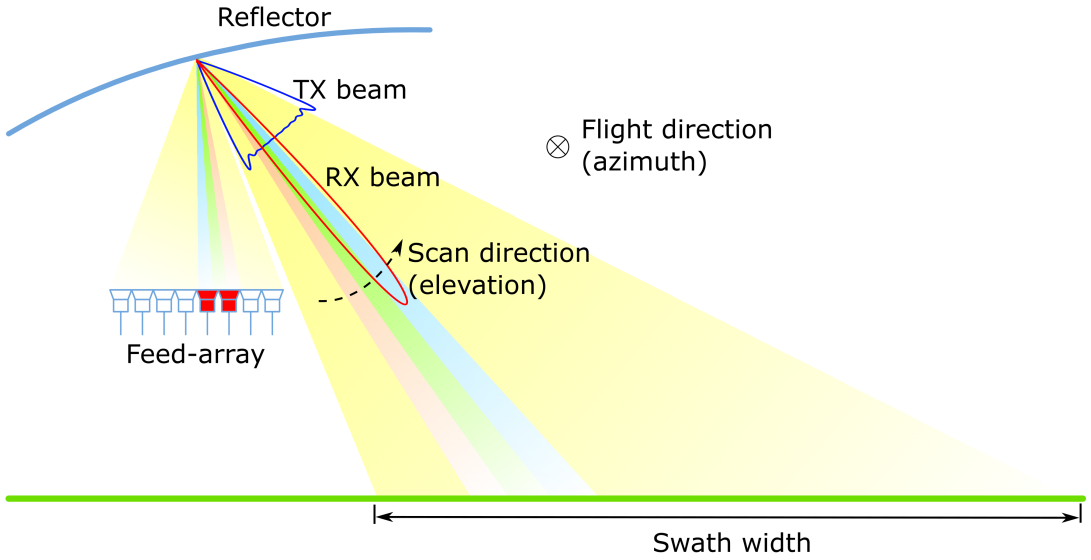

Figure 3.12: Reflector system operation with TX beam shown in yellow and RX beam in different colours for the individual feeds. The RX beam is scanned in elevation along the illuminated swath. Image adapted from [22].

On reception the return echo illuminates the entire reflector surface, resulting in a high-gain signal, with the beam focused on individual feed elements. Beamsteering is performed by selectively switching feeds on and off to correspond with the sub-swaths as the transmitted pulse travels along the ground. For optimum results a number of feeds need to be switched on simultaneously [18], [23], which allows for maximum gain and antenna patterns satisfying the beamwidth requirements. To simplify the modelling in this dissertation, only a single feed element was activated per sub-swath allowing faster validation, but slightly reduced performance.

Figure 3.13 illustrates the reflector configuration specified in [18]. The feed-array consists of 26 elements spaced $d = 0.58\lambda$ apart. Each element was a quadratic $d_f = 0.4\lambda$ patch, resulting in the dimensions for the feed-array of approximately 85 cm $\times$ 5 cm. The reflector had a diameter of $D = 10$ m with a focal length of $F = 5.7$ m. The feed-array was located at the focal point in the z-axis, and orientated along the elevation direction along the x-axis. The paraboloid shape parameter was specified as $a = F/4$.

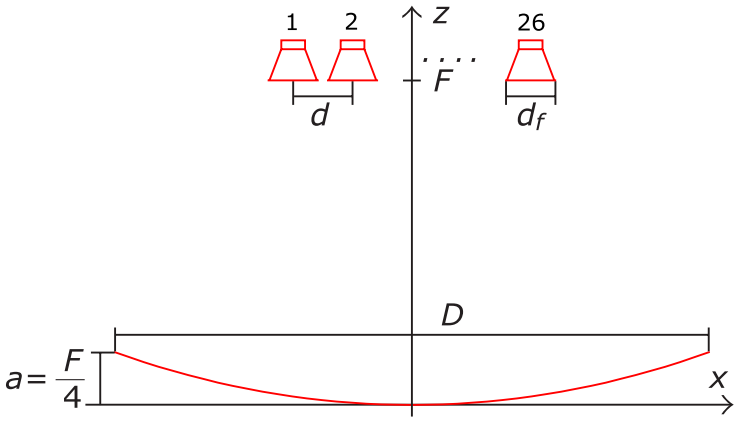

Figure 3.13: C-band reflector and feed-array geometry. The 26-element feed-array is located at the focal point F and orientated in the elevation direction along the x-axis. Image adapted from [18].

Figure 3.14 illustrates the results of the PRF verification step for the C-band reflector system. Similar to Figures 3.1, the choice of PRF is compared against (a) radar altitude, (b) antenna azimuth length, (c) TX pulse length, (d) swath width, (e) incidence angle and (f) look angle, with other fixed parameters listed in Table 3.4. The PRF limits were obtained using Equation 2.30 to Equation 2.34. The choice of system parameters - reflector diameter, feed-array dimensions, number of feeds, focal distance, orbital altitude, transmitter pulse length, swath width, incidence angle range and look angle range - were derived during the initial design phase in [18]. These parameters were chosen to be equivalent to the AESA parameters from [18] presented in Section 3.1.1, for a one-to-one comparison. From these graphs the choice of 1610 Hz for the PRF appears valid. It avoids eclipsing and oversamples the Doppler bandwidth of the scene by a factor of 1610/1507 or 1.07, thus satisfying the requirement of Equation 2.8.

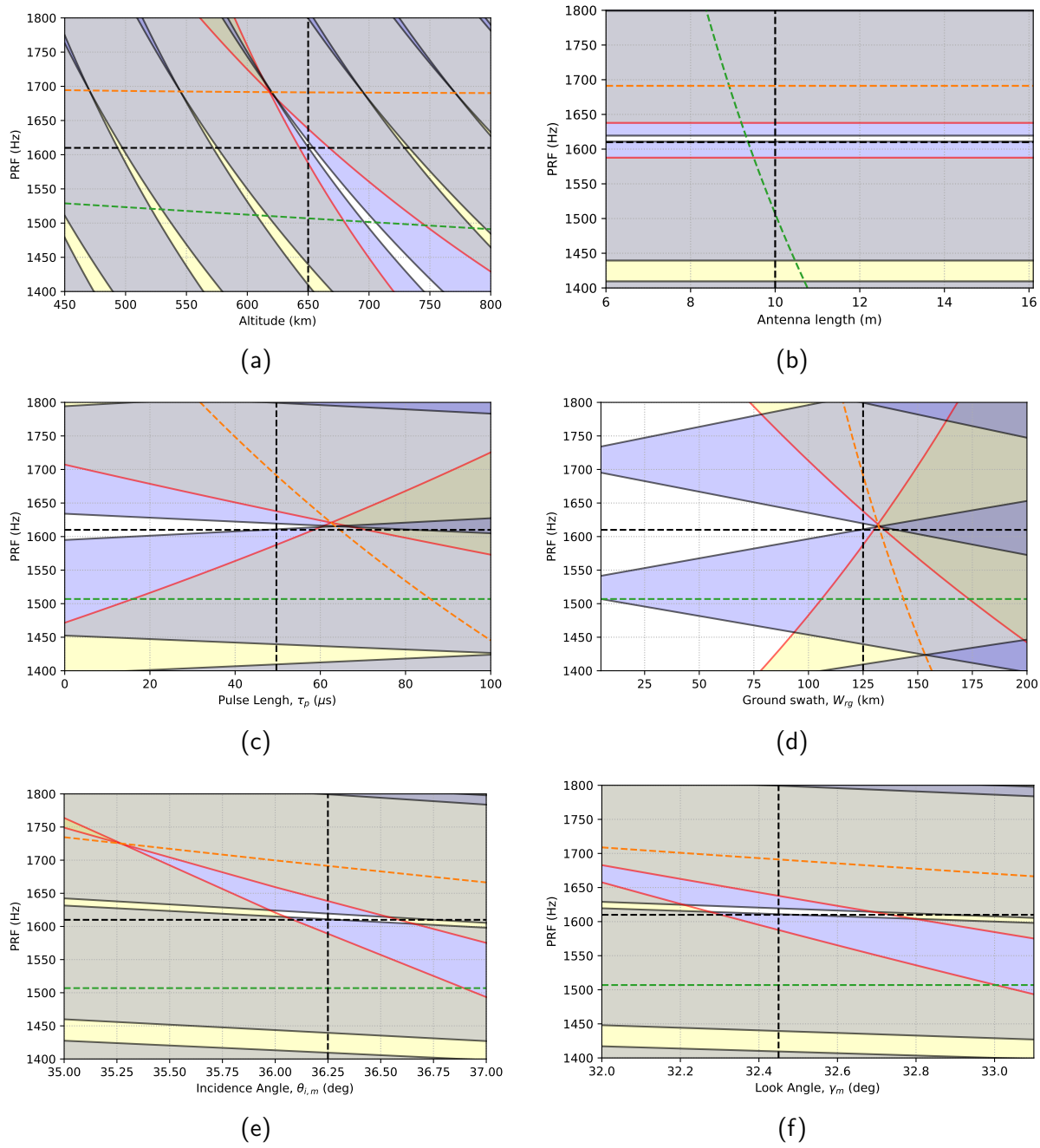

Figure 3.14: C-band reflector system PRF analysis. PRF blind ranges due to transmitter pulse eclipsing are indicated as blue areas between solid black lines, whereas blind ranges due to nadir echo returns are indicated as yellow areas between solid red lines. Valid PRF values are the white spaces between the minimum (green) and maximum (orange) PRF limits. (a) Compares the PRF vs radar altitude. The minimum and maximum PRF decreases with increasing altitude. (b) Compares PRF vs antenna length. PRF maximum is 1691 Hz and PRF minimum decreases with antenna length and is 1507 Hz for a 10 m antenna. (c) Compares PRF vs TX pulse length. PRF maximum decreases with increasing pulse lengths, but PRF minimum is constant at 1507 Hz. (d) Compares PRF vs ground swath. PRF maximum decreases with increasing swaths and PRF minimum is constant at 1507 Hz. (e) Compares PRF vs incidence angle. The PRF is less constrained at smaller incidence angles, with no usable PRFs at incidence angles much larger than 70°. PRF minimum is constant at 1507 Hz, but PRF maximum decreases with increasing incidence angles. (f) Similar to (e), smaller look angles constrain the choice of PRF less and large look angles being less useful. PRF minimum is constant at 1507 Hz and PRF maximum decreases with increasing look angles.

Figure 3.15 illustrates the 3 dB NESZ results for the reflector system calculated using Equation 2.20. The red graphs represent the NESZ values calculated for the 26 individual feed elements, each spaced to cover a different sub-swath of the TX swath. The effective NESZ of the reflector system is shown in green and is simply the trace of the NESZ minima. The NESZ values taper up sharply at the high incidence angles, since they are strongly affected by the TX and RX antenna pattern shapes and slant ranges, however the values lie beneath the -25 dB requirement specified in [18] for the entire swath.

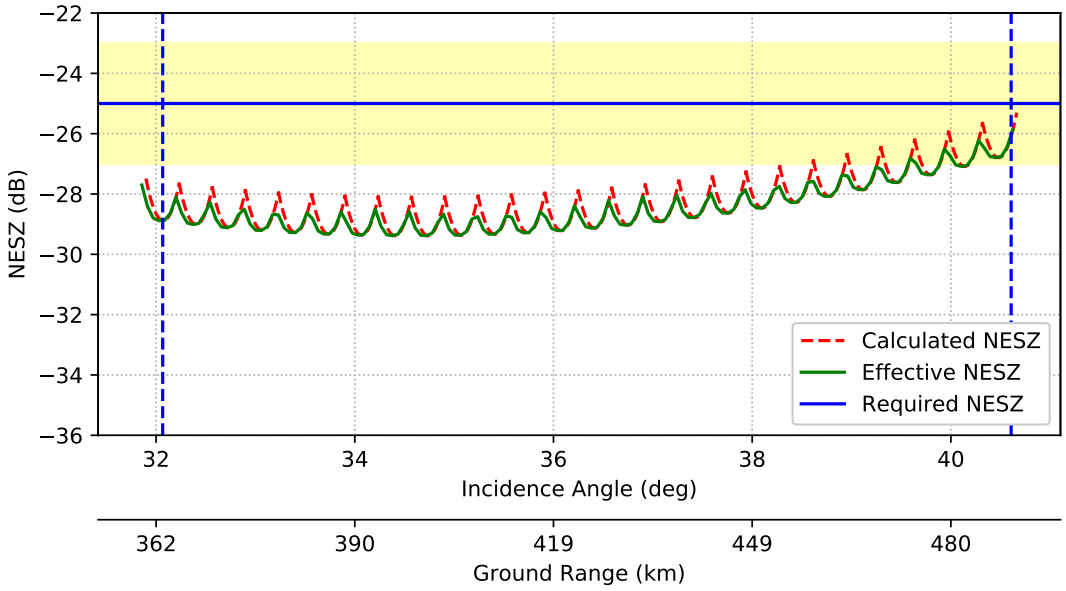

Figure 3.15: Calculated NESZ vs incidence angle for the reflector antenna modelled with the C-band reflector system parameters specified in [18, pp. 8–11]. The required NESZ value is indicated as a solid horizontal blue line with the calculated NESZ values in red. The effective NESZ due to the SCORE operation is shown in green. The incidence angles of interest are indicated between the two dashed vertical blue lines.

Figure 3.16 shows results published in [18, p. 11] for the reflector NESZ over a 125 km swath in stripmap mode. These published results in [18] only depict the scenarios in which two and four feed elements were activated. It specifies in [18, p. 9] that activating individual feeds elements results in a lower gain than when activating two feed elements, but a higher gain than when activating four feed elements. From this it can be inferred that the NESZ values for the single feed element scenario would lie between the two and four feed element scenarios, and therefore would closely match the values obtained in Figure 3.15. A mismatch might occur due to the over-simplification of the antenna aperture model. For more accurate modelling, closed-form field distribution models would need to be utilised.

The published results in [18] were limited to figures, with no exact values specified. Therefore, based on the comparison between Figure 3.15 and Figure 3.16 this verification step was successful.

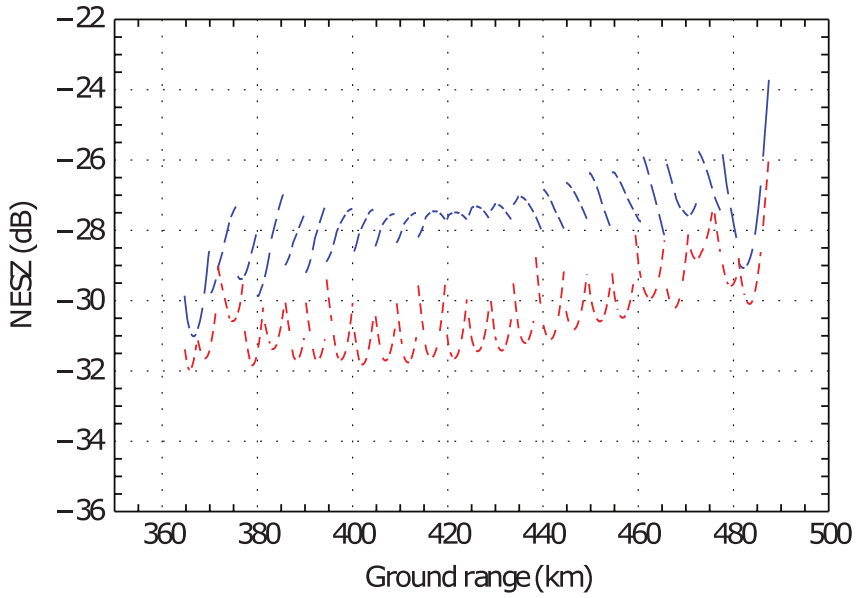

Figure 3.16: Reflector NESZ vs ground range depicted in [18, p. 11] for two (blue) and four (red) active feed elements. This is compared against the calculated values shown in Figure 3.15.

Figure 3.17 illustrate the AASR values for the reflector system obtained using Equation 2.27 for the processed Doppler bandwidth obtained from the orbital velocity, 1255.79 Hz, and from the reduced bandwidth specified in [18], 1150 Hz. From [18] the processed azimuth bandwidth was reduced, at the expense of worsened azimuth resolution, to improve the AASR performance. For the original bandwidth of 1255.79 Hz the AASR was -20.1 dB, which only marginally met the -20 dB requirement. The reduced bandwidth AASR value was approximately -22 dB. The obtained values are constant due to stripmap operation.

Figure 3.18 shows the AASR results from [18, p. 11]. The calculated results are nearly identical to the referenced results, and can be improved even further with antenna tapering applied in azimuth to further reduce the sidelobes.

The published results in [18] were limited to figures, with no exact values specified. Therefore, based on the comparison between Figure 3.17 and Figure 3.18 this verification step was successful.

Note that the calculated AASR result for the reflector system matches the result from the AESA system in Section 3.1.1. This is due to the fact that both antenna systems have the same dimensions in azimuth.

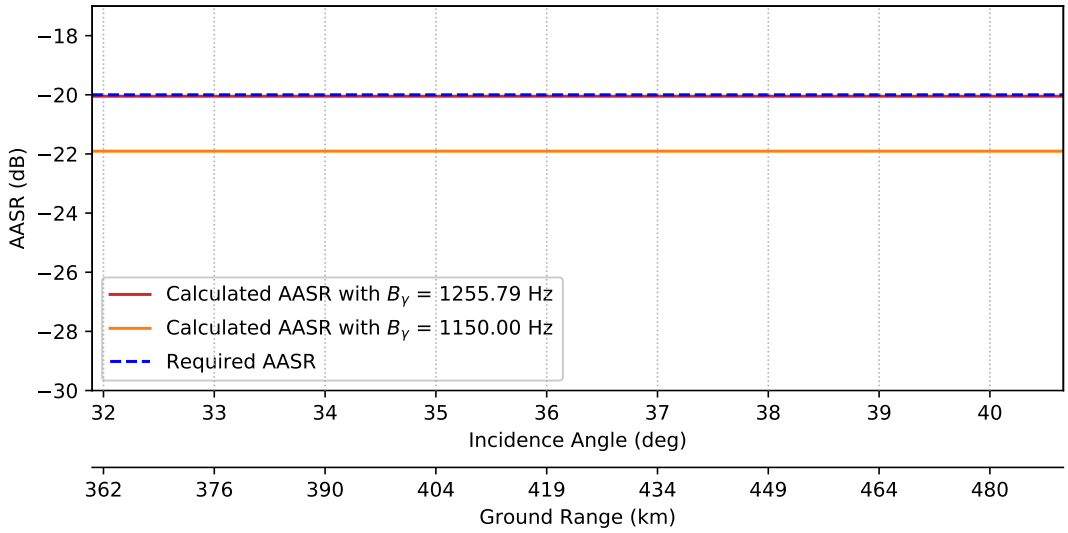

Figure 3.17: Calculated AASR vs slant range for the reflector modelled with the C-band reflector system parameters at the calculated processed Doppler bandwidth [18, pp. 8–1]. The required AASR value is indicated as a dashed horizontal blue line, with the calculated AASR value using a Doppler bandwidth of 1255.8 Hz indicated in red. The calculated AASR with the Doppler bandwidth reduced to 1150 Hz is indicated in orange.

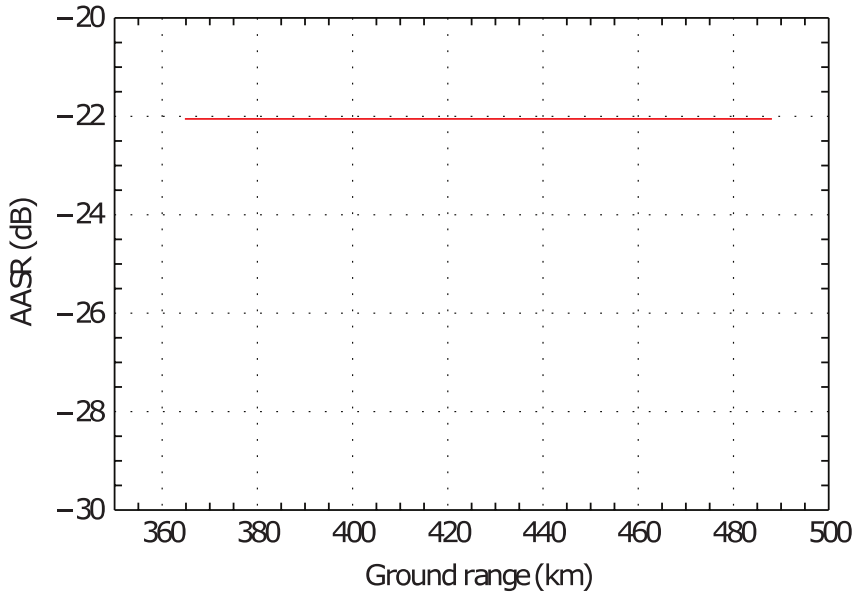

Figure 3.18: Reflector AASR vs ground range depicted in [18, p. 11]. This is compared against the calculated values shown in Figure 3.17.

Figure 3.19 illustrates the RASR values vs incidence angle calculated using Equation 2.25.

Figure 3.20 shows the results from [18, p. 11]. The mismatch between the values in Figure 3.19 and Figure 3.20 can mainly be attributed to the modelling of the antenna pattern. Since no mathematical model for the antenna patterns was specified in [18], a simplified uniformly illuminated rectangular aperture was assumed for the calculations. A more exact field distribution model is required for more accurate modelling of the RASR response. However, the calculated values lie below the required -20 dB level specified in [18].

The published results in [18] were limited to figures, with no exact values specified. Therefore, based on the comparison between Figure 3.19 and Figure 3.20 this verification step was successful.

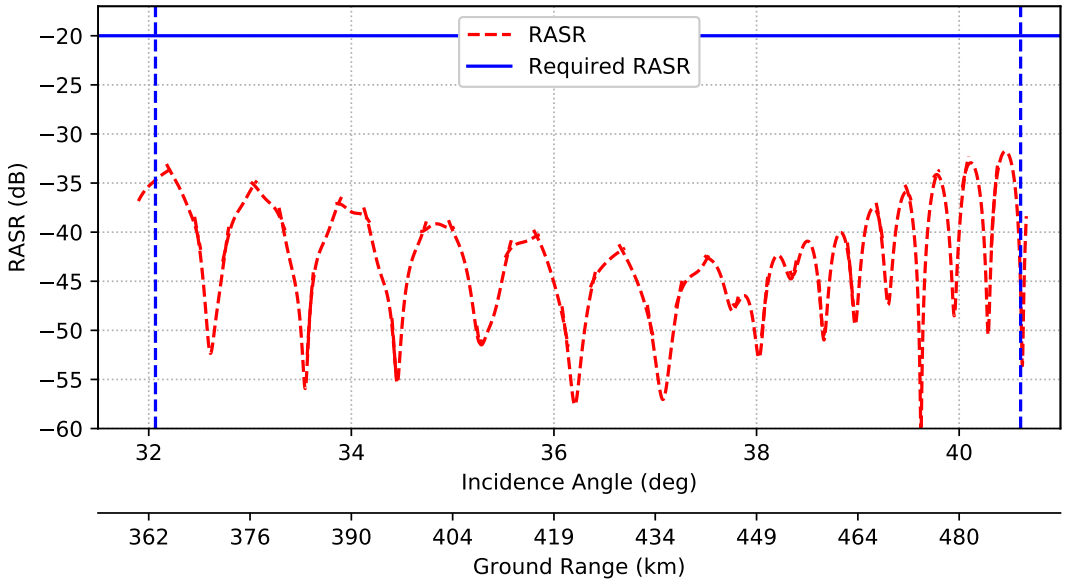

Figure 3.19: Calculated RASR vs incidence angle for the reflector modelled with the C-band system parameters [18, pp. 8–11]. The required RASR value is shown as a solid horizontal blue line, with the calculated RASR in red. The incidence angles of interest lie between the two blue, dashed vertical lines.

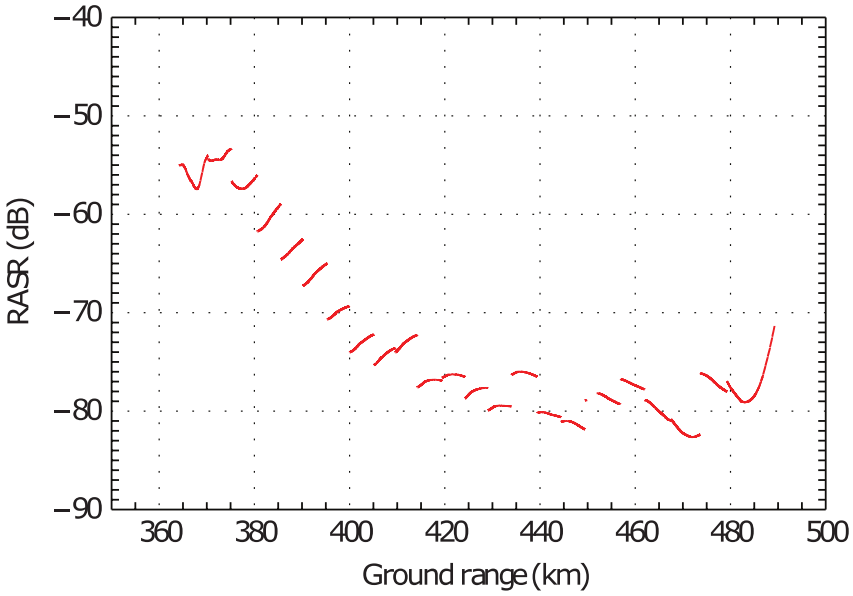

Figure 3.20: Reflector RASR vs ground range depicted in [18, p. 11]. This is compared against the calculated values shown in Figure 3.19.

3.3 Summary

This chapter covered the verification of the Jupyter notebooks and Python modules for modelling and validating the AESA and reflector based systems. To verify the code modules, systems from literature were chosen and modelled as accurately as possible without making unnecessary assumptions of system parameters. The AESA system was modelled and verified against 2 known systems, but due to scarcity of published results, the reflector system was modelled against a single conceptual design.

As an initial step, the choice of PRF was validated against different system parameters to ensure that it falls within the operational limitations imposed by the imaging geometry and characteristics of the radar system and platform. Thereafter the models for NESZ, AASR and RASR were configured and verified. The obtained results correspond closely with published results, with deviations caused by over-simplified modelling of the antenna pattern designs. This means that the software modules and libraries would serve as good first-order rapid system modelling and verification tools.

The next chapter models and compares the performance of an AESA and reflector system with similar specifications.

4 System Design and Performance

The operational use case driving the system design requirements is that of sea ice monitoring. Space-borne SAR systems are useful in monitoring seasonally or permanent ice-covered ocean regions such as those in the northern seas like the Arctic and Baltic Seas [28]. The all-day, all-weather nature of SAR systems allows for the monitoring of diverse and changing properties of sea ice such as ice type, drift, thickness and ice age. Based on previous research, outlined in [28], a set of common system parameters were chosen for the performance comparison of the two radar antenna architectures. This included the choice of incidence angles, required spatial resolution, polarisation, operating frequency and also the required performances in terms of NESZ, AASR and RASR.

A PRF timing analysis was done as a first-order verification step to ensure that the selected frequency, orbital altitude, transmitter duty cycle and resolution will result in a range of PRF values that would:

- Lie between the minimum and maximum PRF
- Cover the required stripmap swath width of at least 70 km
- Ensure the scene return signals do not coincide with the radar transmit events or the nadir echo returns
- Allow the incidence angles to be useful for sea ice monitoring, i.e. between 20° to 49°

With these parameters satisfying the PRF timing constraints, an AESA system and a reflector system were modelled and their performances compared in terms of NESZ, AASR and RASR.

4.1 Shared System Parameters

Figures 4.1 illustrates look angles vs incidence angles for a spherical Earth model at different altitudes. The range of incidence angles useful for sea ice monitoring described in [26], [28] are indicated between the two vertical dashed lines from 20° to 49°. It is evident that there are no useable look angles much larger than 65° and as the altitude increases, this upper limit decreases.

Table 4.1 lists the chosen parameters common to both systems. Table 4.2 lists the performance requirements. C-band was chosen since the radar wavelength can sufficiently penetrate the ice to allow for the distinction between first year and multiyear ice [28]. HH-polarisation helps with the suppression of ocean clutter and is ideal for sea ice mapping applications [28]. The high incidence angles enhances the contrast between smooth level ice and rough ice [28] and this effect is enhanced even more with HH-polarisation. For robust ice type classification the ground resolution needs to be smaller than 10 m [28] and the radar sensitivity needs to be below -20 dB to form usable SAR images [32]. For mapping purposes a wide swath is preferred and imaging methods other than stripmap mode might need to be employed. To simplify the comparison a stripmap mode swath of

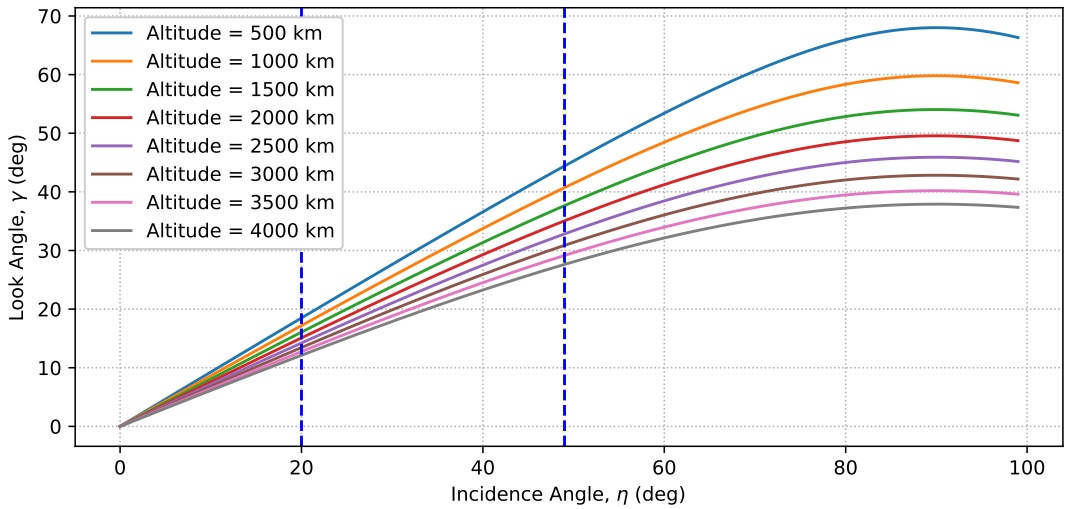

Figure 4.1: Look angle, γ, vs incidence angle, η for a spherical Earth geometry at different orbital altitudes.

at least 70 km is used. As a starting point for the small satellite use case, an upper limit is chosen for the antenna dimensions. The performance of the two antenna architectures is analysed within these constraints and conclusions are drawn on how to further optimise input design parameters. Even though speckle reduction techniques do not form part of this study, these techniques are commonly employed in practice, and therefore the choice of antenna dimensions makes provision for obtaining the required azimuth resolution after multilooking is performed.

For the given orbital altitude, a timing analysis was done to select a PRF which would cover the required swath within the required incidence angle range, and would not coincide with the radar transmit events or with the nadir echo returns.

Table 4.1: Shared SAR system parameters for sea ice monitoring combined from [26], [28].

Parameter	Value	Parameter	Value
Operating Frequency	5.4 GHz	Orbital Altitude	580 km
Incidence Angles	20° - 49°	Resolution	$\leq$ 10 m $\times$ 10 m
Transmitter Duty Cycle	5 %	Polarisation	HH
Max Antenna Length (Az)	$<$ 5 m	Max Antenna Height (El)	$<$ 1 m

Table 4.2: Shared SAR system requirements for sea ice monitoring combined from [26], [28].

Parameter	Value	Parameter	Value
Swath Width	$\geq$ 70 km	NESZ	$\leq$ -20 dB
AASR	$\leq$ -20 dB	RASR	$\leq$ -20 dB

Figure 4.2 indicates that a PRF of 1550 Hz resulted in a receive window over the look angle range of 32.5° to 37°, corresponding to a maximum swath width of 73 km between the ground ranges of 376 km and 449 km. In the simplified stripmap mode with no beamsteering during transmission, the look angle range is equivalent to the transmitter Half Power Beamwidth (HPBW) in elevation $\Theta_{T,el} = 4.5°$. The receiver beamwidth would be different for the planar array and reflector systems.

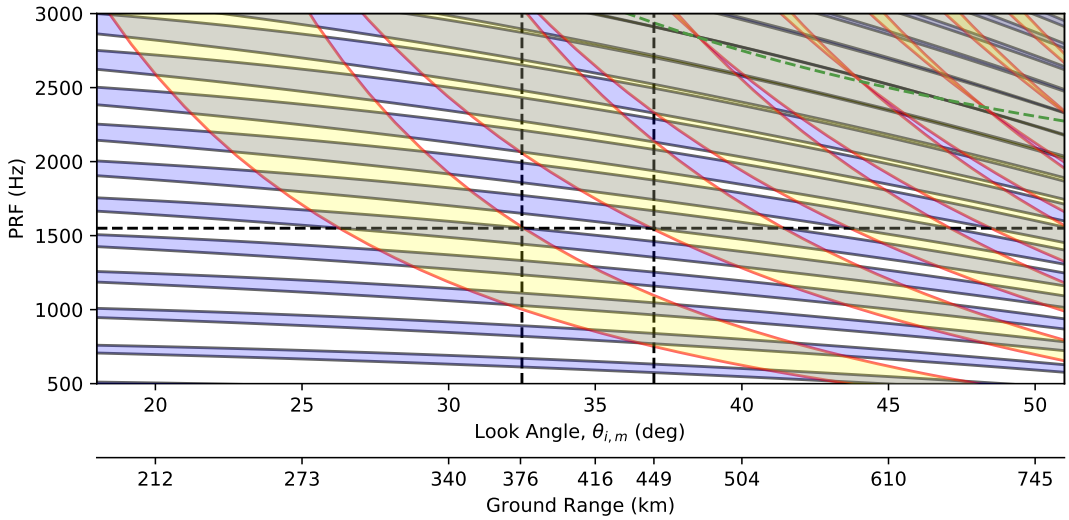

Figure 4.2: Timing diagram for an orbit height of 580 km and a transmit duty cycle of 5 %. The PRF blind ranges due to the transmit events are indicated in blue areas between solid black lines, with nadir echo returns shown as yellow areas between solid red lines. The maximum PRF for the scene duration is indicated in green. The selected PRF and incidence angle range is shown as black dashed lines.

The HPBW in azimuth is derived from the antenna length. An average transmitter power of $P_{avg} = 500W$ is chosen for both systems, together with a duty cycle of 5%.

4.2 Planar Array Properties

The antenna dimensions are determined in elevation by the TX beamwidth required to illuminate the entire swath, and in azimuth by the azimuth ambiguity requirement [18]. The radiating elements for the phased array are spaced $d = 23$ mm apart, which is smaller than $\lambda/2$, so no grating lobes would be visible within the steering range. An arbitrary number of 192 radiating elements in azimtuh are chosen, which results in an antenna azimuth length of 4.416m, which is smaller than the initial 5m upper limit. This azimuth length allows for up to 4 integer looks in azimuth for potential speckle reduction, while still meeting the azimuth resolution requirements. The required $\Theta_{T,el}$ is obtained with 20 elements spaced d apart in elevation. For the receive beam, the antenna height in elevation is further extended, creating a narrower receive beamwidth, whilst increasing the overall antenna gain, ideal for a SCORE operation. An arbitrary number of 35 radiating elements in elevation is chosen, which results in an antenna elevation height of 0.805m, which is smaller than the initial 1m upper

limit. These antenna dimensions are practical in terms of cost and launch vehicle requirements, but might have to be iteratively updated as their performances are analysed. The TX antenna properties are listed in Table 4.3. The RX antenna properties are listed in Table 4.4. The antenna was modelled as an uniformly illuminated aperture with only 64% efficiency, with no tapering applied to suppress sidelobes, so bad azimuth ambiguity performance was expected.

Table 4.3: Derived AESA transmit antenna properties.

Parameter	Value	Parameter	Value
Length	4.416 m	Elevation Beamwidth	4.43°
Height	0.805 m	Azimuth Beamwidth	0.461°
Effective Height	0.437 m	Gain	37.24 dBi
Element Spacing (az x el)	0.023 m $\times$ 0.023 m	Ground Swath	71.4 km
TX Elements (az x el)	192 $\times$ 20	Efficiency	64 %

Table 4.4: Derived AESA receive antenna properties.

Parameter	Value	Parameter	Value
Length	4.416 m	Elevation Beamwidth	2.53°
Height	0.805 m	Azimuth Beamwidth	0.461°
Effective Height	0.805 m	Gain	39.67 dBi
Element Spacing (az x el)	0.023 m $\times$ 0.023 m	Ground Swath	40.74 km
RX Elements (az x el)	192 $\times$ 35	Efficiency	64 %

Figure 4.3 indicates the normalised elevation and azimuth power patterns for the designed planar array antenna.

The results for NESZ, AASR and RASR are shown in Figures 4.5 to 4.7 respectively and compared against the calculated values for the reflector system.

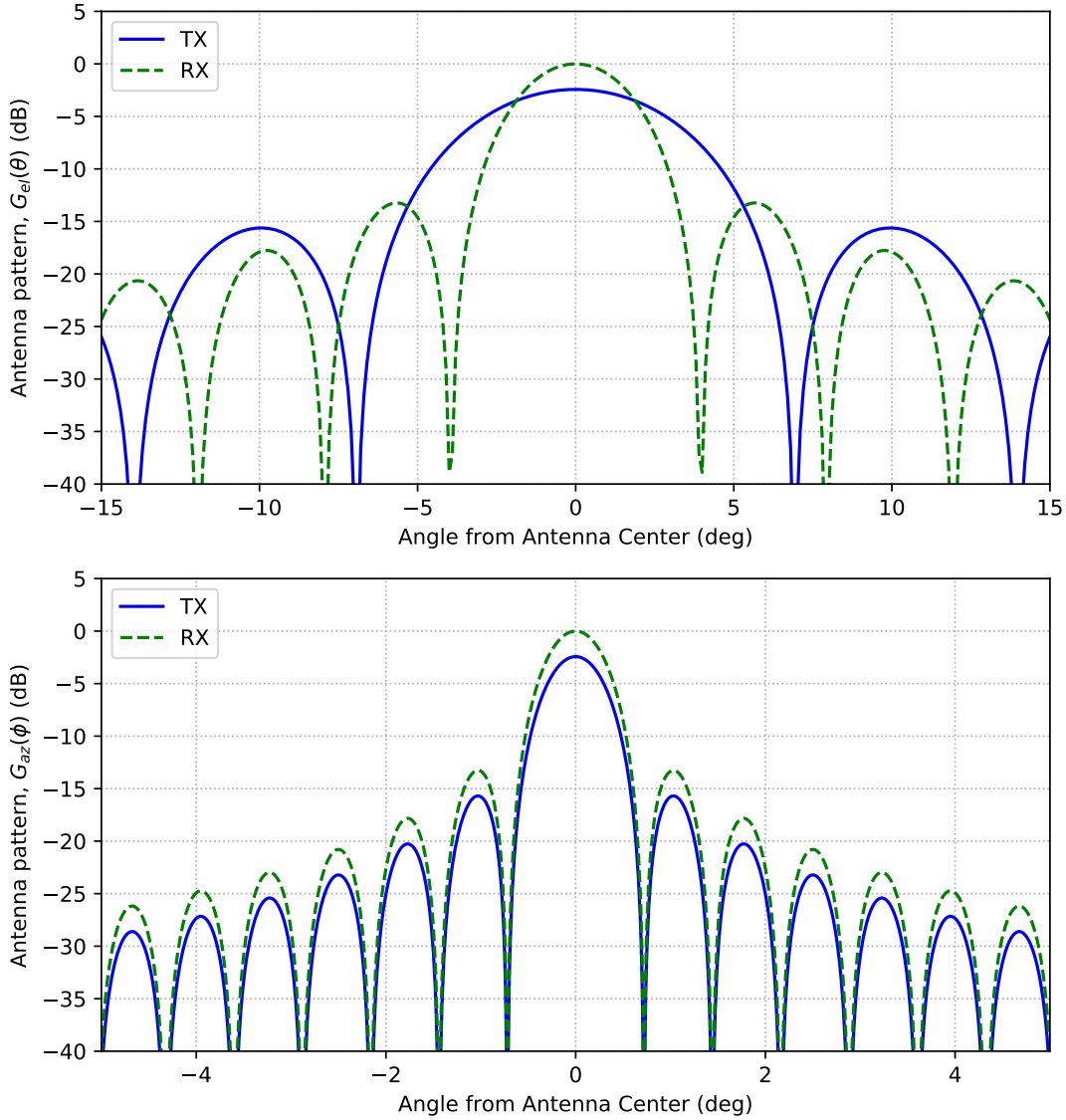

Figure 4.3: Elevation and azimuth power patterns for the planar array antenna design. The power patterns are normalised and scaled according to the gain of the RX antenna. The TX pattern is in blue and the RX pattern in green.

4.3 Reflector Properties

In order to match the performance of the planar array, the reflector system needed to transmit with the same beamwidth in elevation. As a comparable system, the reflector diameter was chosen the same as the planar array length, with a focal length of 2.65 m. A simplified Geometrical Optics approach was used to calculate the feed array length and number of feeds in elevation. The parameters are listed in Table 4.5 and the feeds are spaced $d = 0.51\lambda$ apart with an efficiency of 60%, so there should not be visible grating lobes within the look angle range. During transmission all feeds were activated, resulting in a low gain, broad beam, and feed-blockage was ignored.

On reception, individual feeds were activated to follow the pulse along the ground, but the entire reflector surface was used, so it resulted in a significant receive gain. The parameters are listed in Table 4.6. Each feed illuminates a different sub-swath, with the average width listed in the table.

Table 4.5: Derived reflector transmit antenna properties.

Parameter	Value	Parameter	Value
Diameter	4.416 m	Elevation Beamwidth	4.43°
Sub-aperture Height	0.431 m	Azimuth Beamwidth	0.43°
Feed Spacing (el)	0.03 m	Gain	36.68 dBi
TX Elements (az x el)	1×8	Ground Swath	71.4 km

Table 4.6: Derived reflector receive antenna properties.

Parameter	Value	Parameter	Value
Diameter	4.416 m	Azimuth Beamwidth	0.432°
RX Elements (az x el)	1×1	Gain	45.74 dBi
Elevation Beamwidth	0.553°	Ground Sub-swath	8.35 km

Figure 4.4 indicates the normalised elevation and azimuth power patterns for the designed reflector antenna. The system architecture for the reflector design is similar to that of Figure 3.13, with 8 feeds at the focal point and orientated in elevation along the x-axis. The focal distance, F, is 2.65m.

The results for NESZ, AASR and RASR are shown in Figures 4.5 to 4.7 respectively and are compared against the results for the AESA system.

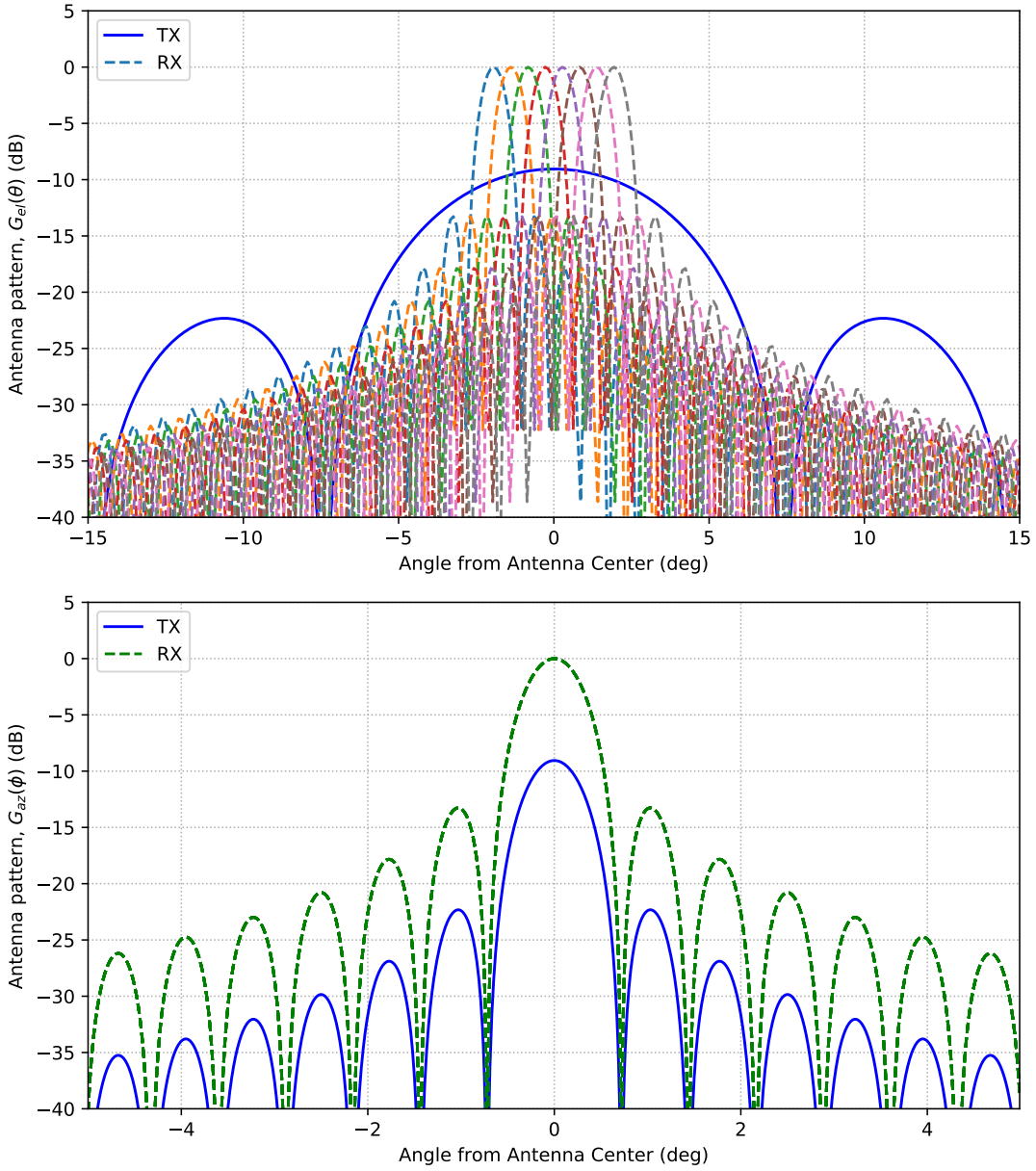

Figure 4.4: Elevation and azimuth power patterns for the reflector antenna design. The power patterns are normalised and scaled according to the gain of the RX antenna. For elevation, the TX pattern is in blue and the RX patterns for each of the 8 feeds are shown. Only a single channel in azimuth is used, and so the RX pattern for all feeds overlap and are shown in green.

4.4 Performance

Figure 4.5 illustrates the NESZ results over the entire incidence angle range for the planar array (a) and reflector system (b), with the values between the dashed vertical blue lines those of interest where, from the PRF analysis, no receiver eclipsing would occur. Refer to Figure 4.2. Both these systems met the sensitivity requirements, however since the reflector made use of its entire surface on reception, its higher gain resulted in a better NESZ response.

Figure 4.6 indicates the AASR results for the two systems. The value are constant over the entire swath due to stripmap mode being used [18]. As predicted, both of these systems suffered from bad azimuth ambiguity performance and neither system met the -20 dB AASR requirement. This is primarily due to the selection of a PRF value, which although sufficient for NESZ and RASR performance requirements, is in fact too low to meet the required AASR performance. Making use of tapering on the azimuth antenna patterns to suppress the sidelobes will significantly improve the AASR response of both systems, but fell outside the scope of this study. Other ways to mitigate the azimuth ambiguities are to make use of higher PRFs, but this would lead to smaller non-eclipsed swaths and a reduced performance in range ambiguity suppression, or to use narrower azimuth beams on transmit and receive. Narrower azimuth beams translates to longer antennas and more phased array elements. This would improve NESZ and RASR as well purely due to the higher gains and transmit power, but a longer antenna on a smallsat class satellite would most likely require complex unfolding mechanisms, requiring more mass and more volume and inevitably increase the cost.

Ultimately there is a coupling between the antenna azimuth length and the choice of PRF. A shorter antenna length would require a higher PRF to improve the AASR performance, and so the design process becomes inherently iterative when optimising for the various performance paramters. Section 4.5 details a recommended workflow to follow when designing towards specified user requirements.

Figure 4.7 illustrates the RASR results for the two systems. Both these systems met the range ambiguity suppression requirements over the incidence angles of interest. It is noticeable that at lower and high incidence angles the RASR performance falls outside of the required range. To mitigate these range ambiguities further a lower PRF would need to be chosen, at the expense of a worse AASR. However, over the angles of interest, the reflector system performed even better than the AESA, due to the high receive gain.

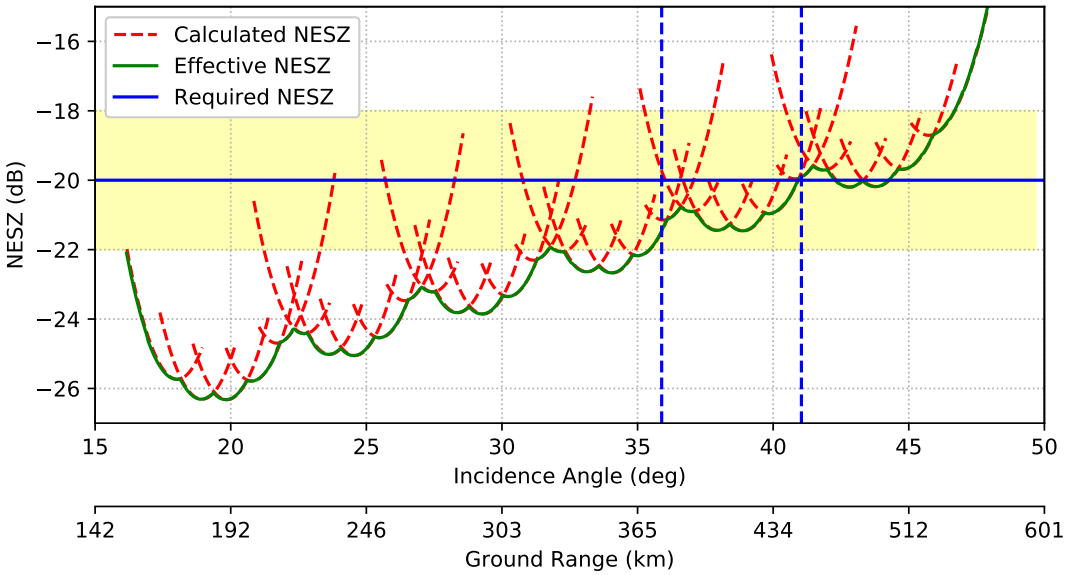

(a)

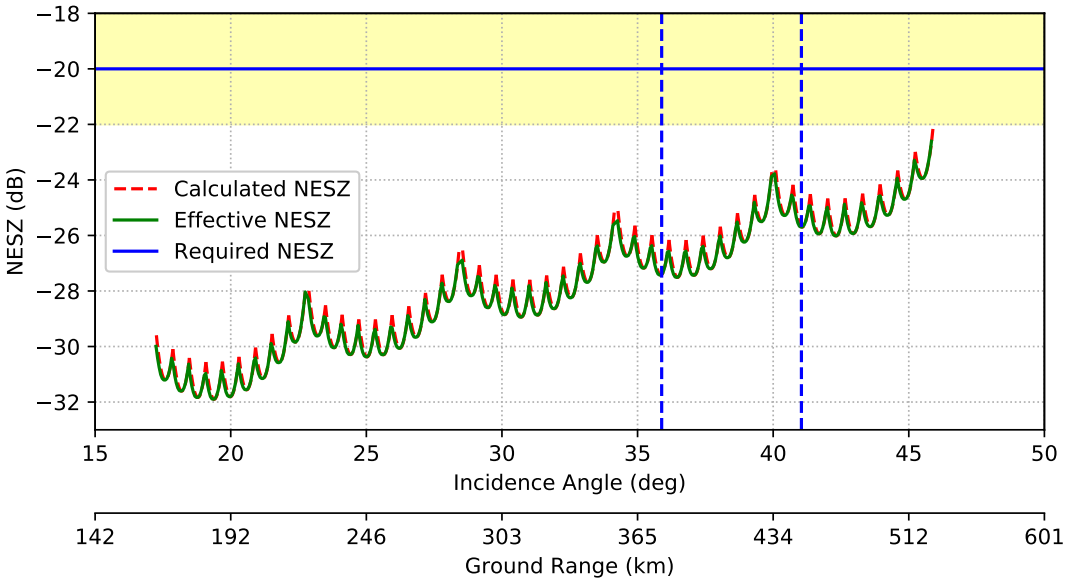

(b)

Figure 4.5: NESZ versus incidence angle for the AESA (a) and reflector systems (b). The required NESZ values is indicated as a solid horizontal blue line, with the calculated NESZ in red. The effective NESZ value for the SCORE operation is shown in green. Values of interest lie between the two dashed vertical blue lines. The yellow area indicates a $\pm 2dB$ range found in some literature since NESZ tends to taper off at the edges of the beam patterns.

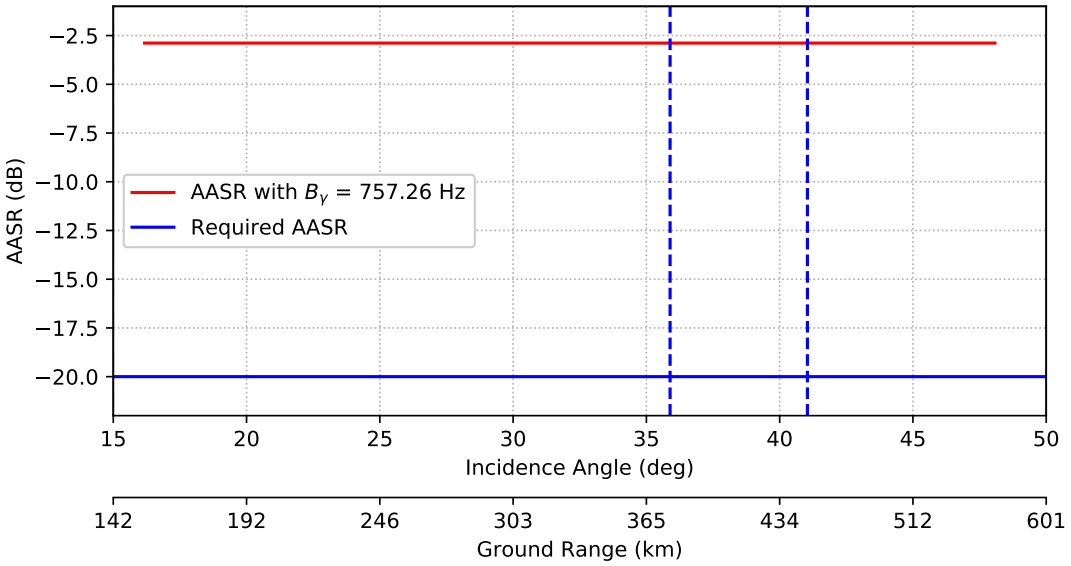

(a)

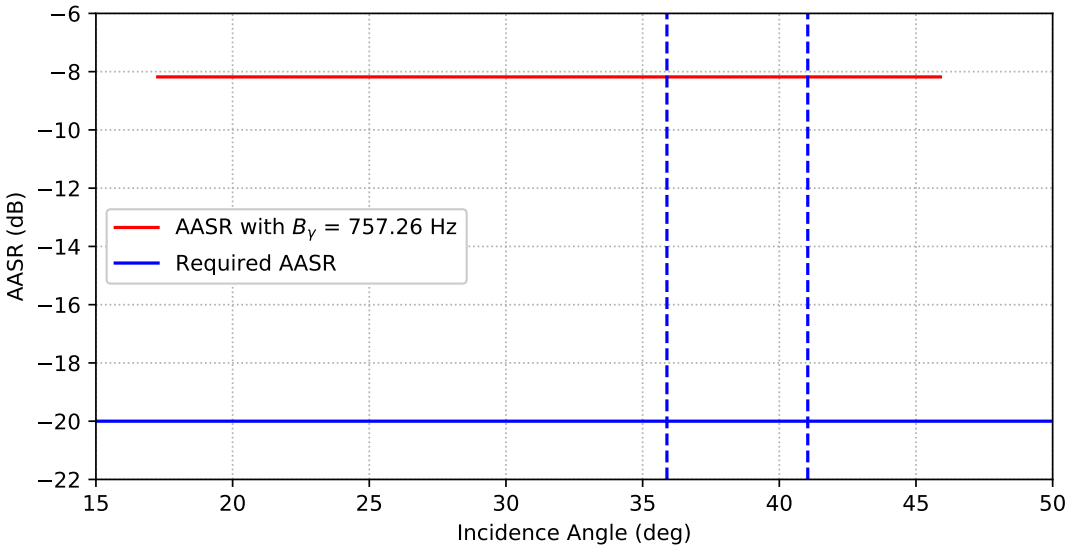

(b)

Figure 4.6: AASR versus incidence angle for the AESA (a) and reflector systems (b). The required AASR value is shown as a solid horizontal blue line with the calculated AASR in red. The AASR response is constant over the swath due to stripmap operation. The processed azimuth bandwidth is calculated as 757.26 Hz. It noted that neither system meets the required AASR performance.

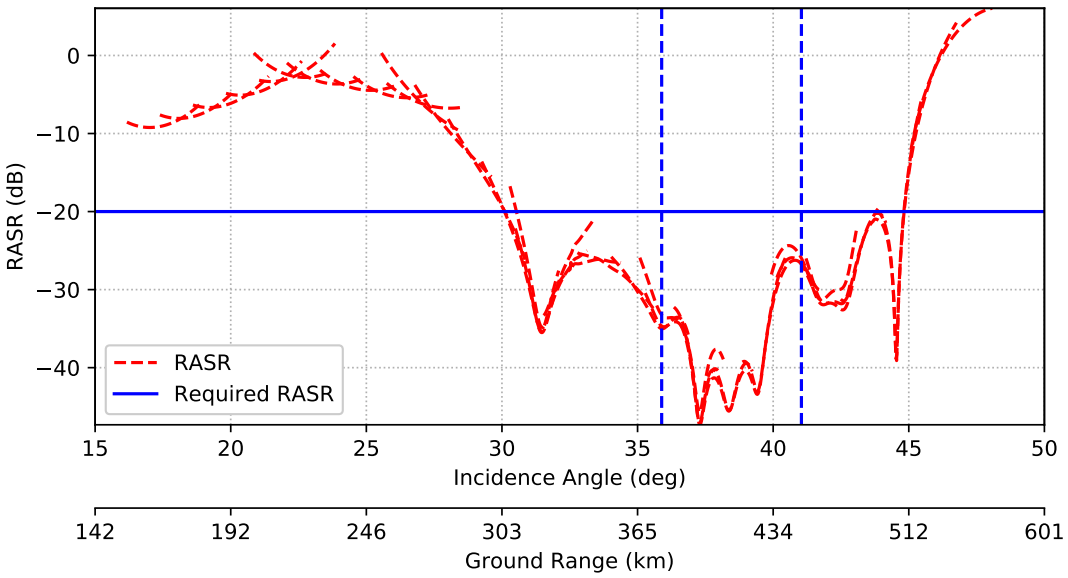

(a)

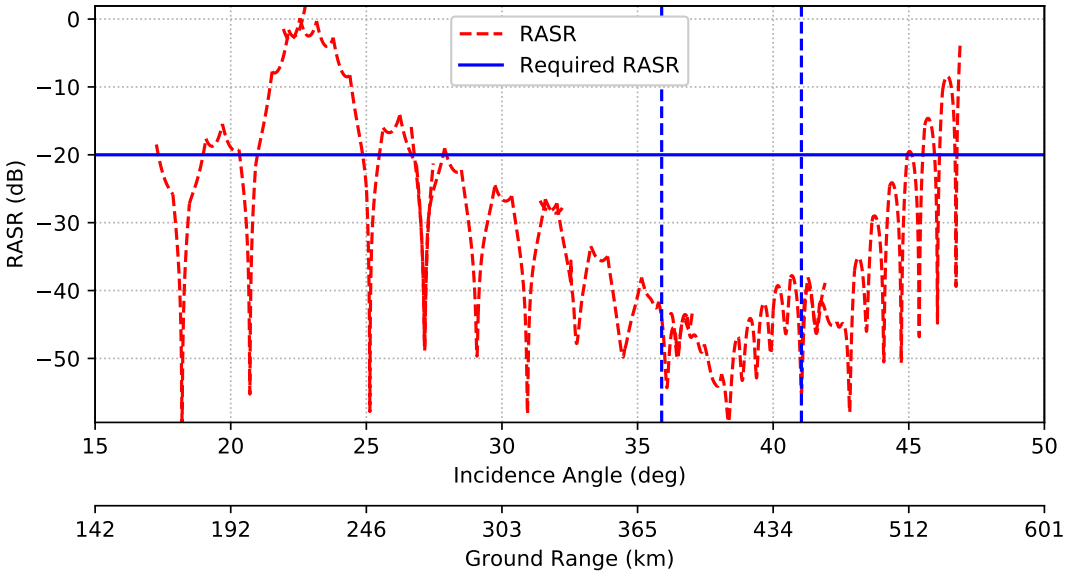

(b)

Figure 4.7: RASR versus incidence angle for the AESA (a) and reflector systems (b). The required RASR value is shown as a solid horizontal blue line with the calculated values in red. Values of interest lie between the two dashed vertical blue lines and both systems meet the requirements, with the reflector performing slightly better.

4.5 Summary and Workflow Recommendation

This chapter presented the case study of sea ice monitoring with which the parameters for the performance comparison were established. Two architectures were considered in this work: a reflector system and an AESA system. The common system parameters and requirements were motivated and validated to fall within the imaging geometry constraints. Parameters obtained from literature included the radar operating frequency, the incidence angles of interest, the spatial resolution, polarisation and performance requirements for NESZ, AASR and RASR. From these a set of system requirements were selected including the SAR platform altitude, the average transmitter power with duty cycle, and the intended swath width.

With these parameters an appropriate PRF was derived using the transmitter duty cycle, the orbital altitude, the imaging swath width and the desired incidence angle ranges. From this the required TX beamwidth and look angle values were obtained and used to design the architecture for the planar array and reflector systems. The chapter proceeded to model the two antenna configurations and presented the respective performance values for comparison.

The reflector system was predicted to have good performance in terms of NESZ and RASR due to the use of a large antenna surface during reception, increasing the receive gain significantly. Both systems were predicted to have bad AASR responses due to the antenna sizes and lack of tapering to the azimuth antenna patterns, and the results confirmed this prediction.

The comparative results indicated that the reflector antenna architecture is a feasible alternative to the AESA architecture for small satellite SAR sensors.

To improve upon the initial design choices for the antenna systems, the PRF selection and the modelling of performance metrics, the workflow illustrated in Figure 4.8 is recommended.

In Figure 4.8 all inputs are defined in blue cells, with derived parameters and output parameters in grey and red cells respectively. In this specific workflow the azimuth and ground range resolutions, together with scene swath width and NESZ performance are system / user requirements. The workflow steps are:

1. Define the basic parameters
    - Platform altitude (h)
    - Look angles (γ) and corresponding incidence angles (η)
    - Radar center frequency (f_0)
    - Polarisation

   1.1 Derive parameters
    - Platform velocity (V_s)
    - Minimum antenna area (A_{eff})

2. User requirements
   - Azimuth resolution (δ_{az})
   - Ground range resolution (δ_{gr})
   - Desired sensitivity ($NESZ$)
   - Desired ambiguity levels ($AASR$, $RASR$)
   - Desired ground swath ($Swath_{max}$)

   2.1 Derive Parameters
   - Pulse bandwidth (B_R)

3. Derive antenna parameters
   - Antenna length (L_{az})
   - Minimum antenna height (H_{el})
   - Antenna beamwidths ($\theta_{az}; \theta_{el}$)
   - Processed azimuth bandwidth (B_p)

4. Derive PRF parameters
   - Maximum pulse duration (τ_p)
   - Minimum PRF (PRF_{min})
   - Maximum PRF (PRF_{max})
   - Valid PRF ranges

5. Calculate ASR ($AASR$ and $RASR$)

   5.1 Choose a valid PRF value that optimises ASR for all incindence angles

   5.2 If ASR requirement not met for all incidence angles, choose a new valid PRF.

   5.3 If no PRF value satisfies the SR requirements, increase the antenna dimensions and repeat Steps 3 - 5

6. Determine sensitivity ($NESZ$)
   - Calculate the TX power (P_{avg}) to satisfy the sensitivity requirement

   6.1 If the sensitivity requirement is not met, then some of the system or user requirements need to be relaxed. Go to Step 2 and change either resolution or swath requirements. Repeat Steps 2 - 6.

Appendix B illustrates the relationship and dependencies between the various SAR parameters.

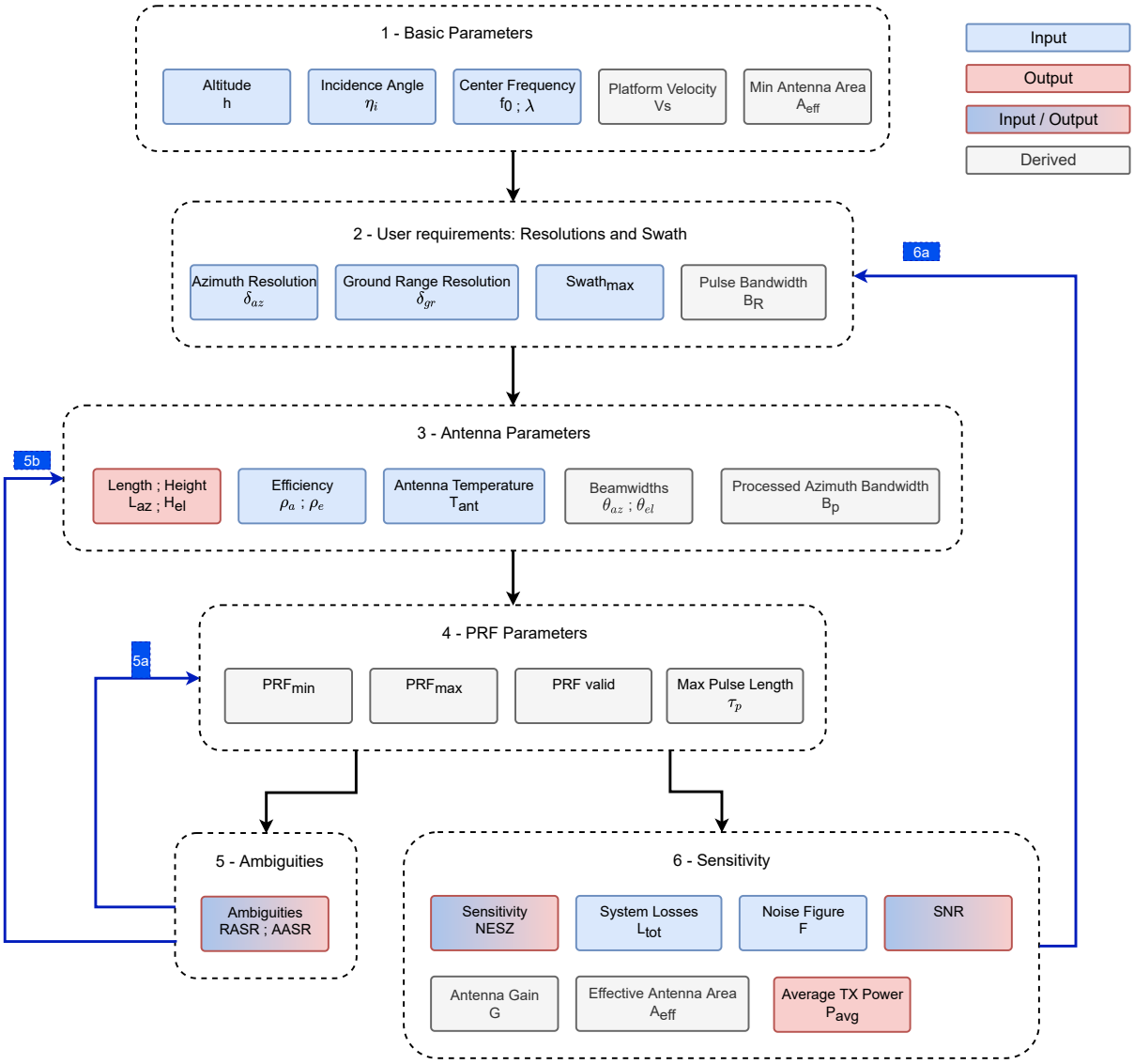

Figure 4.8: Spaceborne SAR sensor design workflow with fixed resolution, swath and NESZ requirements.

5 Conclusions

The application field and commercial use cases for spaceborne SAR systems and the data they generate are expanding. Business models are being developed around the manufacturing and commercialisation of small satellite SAR sensors. These aim to perform a variety of Earth observation functions, from multi-satellite surveillance constellations to dedicated asset monitoring and route mapping. The first commercial small satellite SAR demonstrators were launched and commissioned in 2018, one operating in S-band and the other in X-band. These demonstrators built upon decades of research in spaceborne SAR sensors and confirmed the viability and performance of a smaller class sensor.

The performance drivers for SAR systems in terms of SNR and NESZ are principally the transmitter power and the antenna gain. With planar array antennas, utilising a multitude of TRMs, to increase the transmitted power or antenna gain means to further increase the number of transmit elements in both antenna dimensions. This exponential increase in elements also means an exponential increase in manufacturing cost. In this work the performance of reflector antenna designs was compared against that of planar array antennas.

The concept of using a large reflector surface to increase the antenna gain, and the use of a small number of feed elements was investigated as an alternative to a similarly sized planar array. DBF and SCORE techniques were employed to fulfil the use case requirements of wide swath coverage at high spatial resolution. This work was based on the research done by Younis et al. in [18], and aimed at implementing the required software models to design and verify different configurations for reflector and planar array systems. The implemented software models were verified to correspond closely to published results.

Previous research done in the field of spaceborne SAR systems indicated that the proper design of the antenna is crucial to avoid distortions to the imaged scene caused by ambiguous signal returns. These ambiguities are present in both the azimuth and the range directions. The antenna dimensions, sidelobe tapering and the PRF selection were the main contributors to the successful suppression of these ambiguities.

A PRF timing analysis was done to determine the influence of the spherical Earth model on the choices of orbital altitude, antenna azimuth length, transmitter pulse length, swath width, incidence angles and look angle ranges. From the resulting parameters a planar array and reflector system were modelled and compared in terms of NESZ, AASR and RASR. The modelled systems in this work corresponded with the published performance results, and indicated that reflector systems are indeed a feasible alternative for small satellite SAR sensors.

To improve upon this study, more accurate modelling of the antenna patterns and their field distri-

butions is needed. For the reflector system this would include the modelling of the reflector surface, feed placement and feed blockage effects. To further expand on the software utilities as a workable system to model and verify system designs, the ScanSAR and Spotlight operational modes are to be added.

Active research is being done on the use of large unfoldable mesh reflectors combined with digital feed arrays for future SAR systems. The use of these antennas would reduce the constraints of launch vehicle volume and mass, and could therefore potentially outperform existing larger planar arrays in terms of NESZ and range ambiguity suppression.

Appendix A: Code Listing

The code for the Jupyter notebooks and Python libraries are available on GitHub here:

https://github.com/azheikg/masters_jupyter

Appendix B: SAR Parameter Relationship

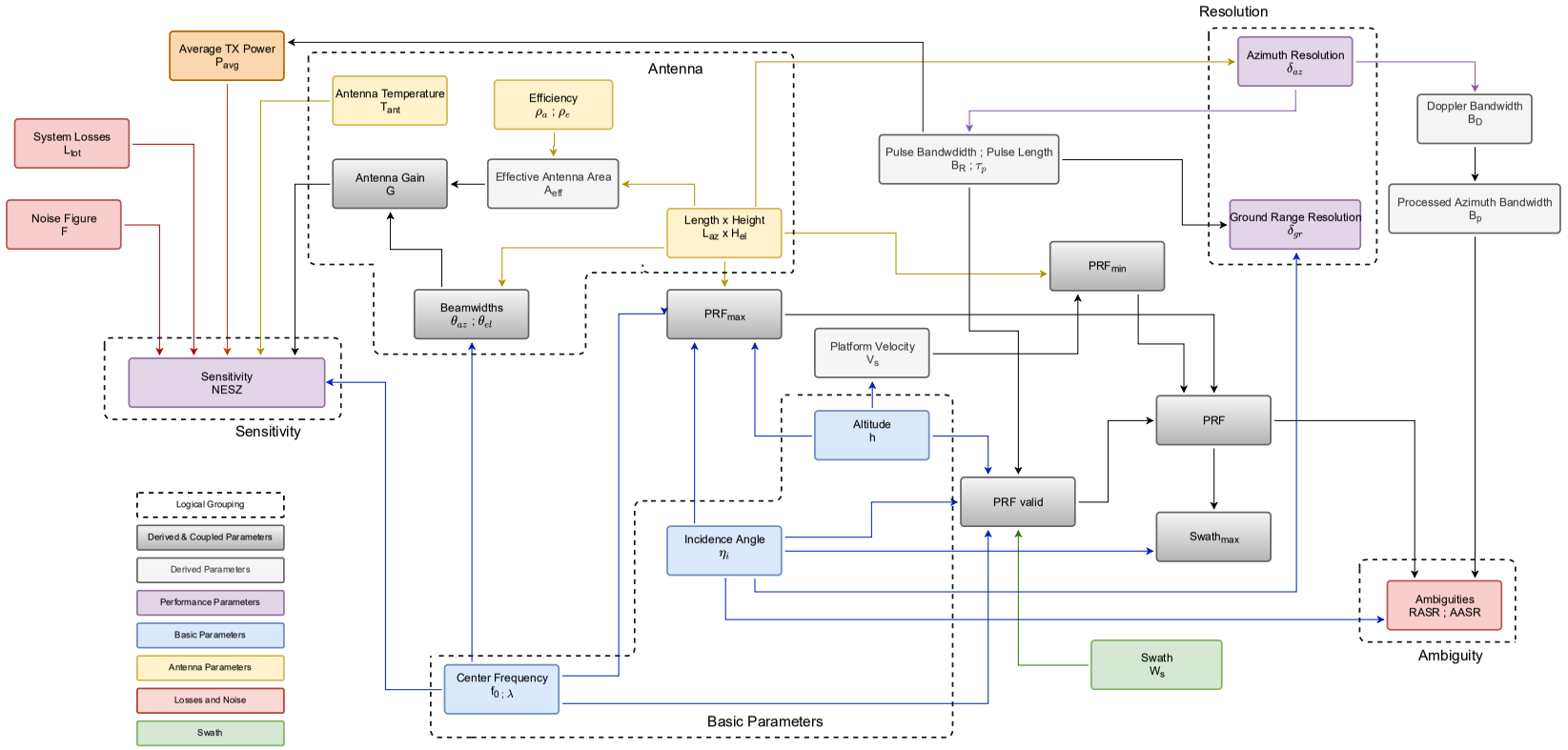

Figure 5.1: Spaceborne SAR parameter relationship and dependencies.

Bibliography

[1] R. L. Jordan, "The Seasat-A Synthetic Aperture Radar System," *IEEE Journal of Oceanic Engineering*, vol. 5, pp. 154–164, 1980.

[2] E. O. Portal. (2018). Seasat Mission — the World's First Satellite Mission Dedicated to Oceanography, [Online]. Available: https://directory.eoportal.org/web/eoportal/satellite-missions/s/seasat (visited on 09/20/2018).

[3] ——, (2018). SIR-A (Shuttle Imaging Radar) / OSTA-1 Payload on STS-2 Mission, [Online]. Available: https://directory.eoportal.org/web/eoportal/satellite-missions/s/sir-a (visited on 09/20/2018).

[4] J. Cimino, C. Elachi, and M. Settle, "SIR-B - The Second Shuttle Imaging Radar Experiment," *IEEE Transactions on Geoscience and Remote Sensing*, vol. GE-24, no. 4, pp. 45–452, Jul. 1986.

[5] E. O. Portal. (2018). SIR-C/X - SAR Payload on STS-59 and STS-68 Missions, [Online]. Available: https://directory.eoportal.org/web/eoportal/satellite-missions/s/sir-c (visited on 09/21/2018).

[6] R. Petersson and P. Ingvarson, "The Planar Array Antennas for the European Remote Sensing Satellite ERS-1," presented at the 1988 18th European Microwave Conference, Sep. 1988.

[7] M. Rast, "ESA's Future Plans for Earth Observation from Polar Orbit," presented at the Proceedings of IGARSS '94 - 1994 IEEE International Geoscience and Remote Sensing Symposium, vol. 4, Aug. 1994, pp. 1705–1708.

[8] V. S. Verba, L. B. Neronskiy, and I. Osipov, "Russian Spaceborne Imaging Radars : Scientific and Technical Achievements and Priority Perspectives of Development," 2005.

[9] E. O. Portal. (2018). JERS-1 (Japan Earth Resources Satellite) / Fuyo-1, [Online]. Available: https://directory.eoportal.org/web/eoportal/satellite-missions/j/jers-1 (visited on 09/21/2018).

[10] M. Werner, "Shuttle Radar Topography Mission (SRTM): Experience With the X-band SAR Interferometer," presented at the 2001 CIE International Conference on Radar Proceedings (Cat No.01TH8559), Oct. 2001, pp. 634–638.

[11] J. Louet and S. Bruzzi, "ENVISAT Mission and System," presented at the IEEE 1999 International Geoscience and Remote Sensing Symposium. IGARSS'99 (Cat. No.99CH36293), vol. 3, Jun. 1999, pp. 1680–1682.

[12] L. Brule, D. Delisle, H. Baeggli, and J. Graham, "RADARSAT-2 Program Update," presented at the Proceedings. 2005 IEEE International Geoscience and Remote Sensing Symposium, 2005. IGARSS '05. Vol. 1, Jul. 2005, p. 3.

[13] S. Buckreuss, R. Werninghaus, and W. Pitz, "The German Satellite Mission TerraSAR-X," presented at the 2008 IEEE Radar Conference, May 2008, pp. 1–5.

[14] A. Moreira, G. Krieger, I. Hajnsek, D. Hounam, M. Werner, S. Riegger, and E. Settelmeyer, "TanDEM-X: a TerraSAR-X Add-on Satellite for Single-pass SAR Interferometry," presented at the IGARSS 2004. 2004 IEEE International Geoscience and Remote Sensing Symposium, vol. 2, Sep. 2004, pp. 1000–1003.

[15] NASA. (2018). Cassini – Solar System Exploration: NASA Science, [Online]. Available: https://solarsystem.nasa.gov/missions/cassini/mission/spacecraft/cassini-orbiter/radio-detection-and-ranging/ (visited on 09/25/2018).

[16] ESA. (2018). SAR-Lupe Constellation, [Online]. Available: https://earth.esa.int/web/eoportal/satellite-missions/s/sar-lupe (visited on 09/25/2018).

[17] ——, (2018). TecSAR (SAR Technology Demonstration Satellite), [Online]. Available: https://earth.esa.int/web/eoportal/satellite-missions/t/tecsar (visited on 06/26/2018).

[18] M. Younis, S. Huber, A. Patyuchenko, F. Bordoni, and G. Krieger, "Performance Comparison of Reflector- and Planar-Antenna Based Digital Beam-Forming SAR," *International Journal of Antennas and Propagation*, vol. 2009, pp. 1–13, 2009.

[19] F. Bordoni, M. Younis, E. M. varona, N. Gebert, and G. Krieger, "Performance Investigation on Scan-on-Receive and Adaptive Digital Beam-forming for High-Resolution Wide-swath Synthetic Aperture Radar," presented at the Proceedings of the International ITG Workshop of Smart Antennas, Feb. 2009, pp. 114–121.

[20] N. Gebert, G. Krieger, and A. Moreira, "Digital Beamforming on Receive: Techniques and Optimization Strategies for High-Resolution Wide-Swath SAR Imaging," *IEEE Transactions on Aerospace and Electronic Systems*, vol. 45, no. 2, pp. 564–592, Apr. 2009.

[21] M. van den Oever, "Space-Based FMCW SAR Systems," MSc. thesis, Delft University of Technology, Delft, Netherlands, 2012.

[22] S. Huber, "Spaceborne SAR Systems with Digital Beamforming and Reflector Antenna," Dr.-Ing, Karlsruhe Institute of Technology, Augsburg, Germany, Feb. 2014. [Online]. Available: https://elib.dlr.de/76420/1/Dissertation_Huber.pdf.

[23] S. Huber, M. Younis, A. Patyuchenko, G. Krieger, and A. Moreira, "Spaceborne Reflector SAR Systems with Digital Beamforming," *IEEE Transactions on Aerospace and Electronic Systems*, vol. 48, no. 4, pp. 3473–3493, Oct. 2012.

[24] E. O. Portal. (2018). Tandem-L Interferometric Radar Mission, [Online]. Available: https://directory.eoportal.org/web/eoportal/satellite-missions/t/tandem-l (visited on 06/26/2018).

[25] P. Jupyter. (). Project Jupyter, [Online]. Available: http://www.jupyter.org (visited on 07/16/2018).

[26] C. Livingstone, C. Sikaneta, S. Gierull, M. P. Chiu, and Beaulne, "RADARSAT-2 System and Mode Description," Dec. 2018.

[27] *RADARSAT-2 Product Description*, RN-SP-52-1238, Issue 1/14, MDA Corporation, Sep. 2018.

[28] W. Dierking, "Sea Ice Monitoring by Synthetic Aperture Radar," *Oceanography*, vol. 26, no. 2, pp. 100–111, Jun. 2013. [Online]. Available: https://doi.org/10.5670/oceanog.2013.33.

[29] L. Eriksson, K. Borenäs, W. Dierking, A. Berg, M. Santoro, P. Pemberton, H. Lindh, and B. Karlson, "Evaluation of new spaceborne SAR sensors for sea-ice monitoring in the Baltic Sea," *Canadian Journal of Remote Sensing*, vol. 36, pp. 56–73, Jan. 2010.

[30] M. A. Richards, W. A. Holm, and J. Scheer, *Principles of Modern Radar: Basic Principles*. Institution of Engineering and Technology, 2010.

[31] Y.-J. Won, K. H. Lee, and J.-H. Lee, "Performance Improvement of Spaceborne SAR Using Antenna Pattern Synthesis Based on Quantum-Behaved Particle Swarm Optimization," *International Journal of Antennas and Propagation*, vol. 2017, pp. 1–12, 2017.

[32] J. C. Curlander and R. N. McDonough, *Synthetic Aperture Radar - Systems And Signal Processing*. John Wiley & Sons, Inc., 1991.

[33] I. Elizavetin. (2010). Radiometric Artifacts on SAR Images, [Online]. Available: http://www.racurs.ru/download/conf/Italy2010/Presentations/Elizavetin.pdf (visited on 09/29/2018).

[34] X. Leng, K. Ji, S. Zhou, X. Xing, and H. Zou, "An Adaptive Ship Detection Scheme for Spaceborne SAR Imagery," *Sensors*, vol. 16, no. 9, 2016.

[35] R. Scheiber and M. Jaeger, "Detection and Mitigation of Strong Azimuth Ambiguities in High Resolution SAR Images," presented at the Proceedings of EUSAR 2016: 11th European Conference on Synthetic Aperture Radar, Jun. 2016.

[36] S. Gharibi and J. Amini, "Detection and Analysis of Appropriate PRF for Spaceborne SAR Sensors," Aug. 2012.

[37] P. Rizki Akbar, J. Tetuko S. S, and H. Kuze, "A Novel Circularly Polarized Synthetic Aperture Radar (CP-SAR) System Onboard a Spaceborne Platform," *International Journal of Remote Sensing*, vol. 31, no. 2, pp. 1053–1060, Feb. 2010.

[38] D. L. Bickel, B. C. Brock, and C. T. Allen, "Spaceborne SAR study: LDRD '92 final report," Mar. 1993.

[39] J. Mittermayer, M. Younis, R. Metzig, S. Wollstadt, J. M. Martinez, and A. Meta, "TerraSAR-X System Performance Characterization and Verification," *IEEE Transactions on Geoscience and Remote Sensing*, vol. 48, no. 2, pp. 660–676, Feb. 2010.

[40] Michelangelo Villano and Gerhard Krieger and Alberto Moreira, "Waveform-Encoded SAR: A Novel Concept for Nadir Echo and Range Ambiguity Suppression," in *European Conference on Synthetic Aperture Radar (EUSAR)*, Jun. 2018. [Online]. Available: https://elib.dlr.de/119286/.